

## **INFORMATION TO USERS**

This manuscript has been reproduced from the microfilm master. UMI films the text directly from the original or copy submitted. Thus, some thesis and dissertation copies are in typewriter face, while others may be from any type of computer printer.

**The quality of this reproduction is dependent upon the quality of the copy submitted.** Broken or indistinct print, colored or poor quality illustrations and photographs, print bleedthrough, substandard margins, and improper alignment can adversely affect reproduction.

In the unlikely event that the author did not send UMI a complete manuscript and there are missing pages, these will be noted. Also, if unauthorized copyright material had to be removed, a note will indicate the deletion.

Oversize materials (e.g., maps, drawings, charts) are reproduced by sectioning the original, beginning at the upper left-hand corner and continuing from left to right in equal sections with small overlaps. Each original is also photographed in one exposure and is included in reduced form at the back of the book.

Photographs included in the original manuscript have been reproduced xerographically in this copy. Higher quality 6" x 9" black and white photographic prints are available for any photographs or illustrations appearing in this copy for an additional charge. Contact UMI directly to order.

**UMI<sup>®</sup>**

**Bell & Howell Information and Learning  
300 North Zeeb Road, Ann Arbor, MI 48106-1346 USA  
800-521-0600**

DISSERTATION

IONIZED MAGNETRON SPUTTERING OF  $Al_2O_3$

Submitted by

Patrick F. Gonzalez

Electrical Engineering Department

In partial fulfillment of the requirements

For the Degree of Doctor of Philosophy

Colorado State University

Fort Collins, Colorado

Spring 2000

UMI Number: 9981332

UMI<sup>®</sup>

---

UMI Microform 9981332

Copyright 2000 by Bell & Howell Information and Learning Company.

All rights reserved. This microform edition is protected against  
unauthorized copying under Title 17, United States Code.

---

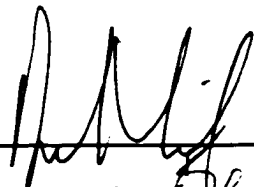
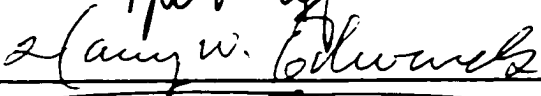
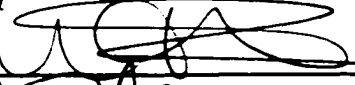
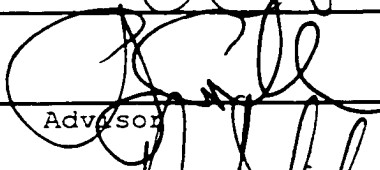
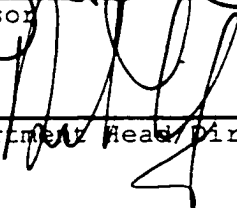
Bell & Howell Information and Learning Company  
300 North Zeeb Road  
P.O. Box 1346  
Ann Arbor, MI 48106-1346

COLORADO STATE UNIVERSITY

February 18<sup>th</sup>, 2000

WE HEREBY RECOMMEND THAT THIS DISSERTATION PREPARED UNDER OUR SUPERVISION BY PATRICK F. GONZALEZ ENTITLED "IONIZED MAGNETRON SPUTTERING OF Al<sub>2</sub>O<sub>3</sub>" BE ACCEPTED AS FULFILLING IN PART THE REQUIREMENTS FOR THE DEGREE OF DOCTOR OF PHILOSOPHY

Committee on Graduate Work

  
\_\_\_\_\_  
*Patrick F. Gonzalez*  
\_\_\_\_\_  
  
\_\_\_\_\_  
  
\_\_\_\_\_  
  
\_\_\_\_\_  
Advisor  
  
\_\_\_\_\_  
Department Head/Director

## ABSTRACT OF DISSERTATION

### IONIZED MAGNETRON SPUTTERING OF $\text{Al}_2\text{O}_3$

This dissertation shows a detailed study of the conditions necessary for sputtering alumina using a novel variant of ionized magnetron sputtering (IMS) first demonstrated by Yamashita et. al. The study presented herein leverages concurrent research at our laboratory on high density plasmas, plasma characterization and charged particle beams research to demonstrate a new source capable of sputtering hydrated alumina films at high rates.

High quality ceramics such as  $\text{Al}_2\text{O}_3$  find uses in a variety of applications, and in particular, for mass storage applications. Consequently, there exists an ever-growing need to provide and improve the capability of growing thick insulating films. Ideally, the insulating film should be stoichiometric and able to be grown at rates high enough to be easily manufacturable. Alumina is a particularly attractive due to its high density, Na barrier properties, and stability and radiation resistance.

However, high quality films are often difficult to achieve with conventional RF plasma due to extremely slow deposition rates and difficulties associated with system cooling. The preferred method is to reactively sputter Al from a solid target in an  $\text{O}_2$  ambient. Nevertheless, this process is inherently unstable and leads to arcing and uneven target wear when magnetrons are used.

In this study, we build the sputtering source, evaluate, and maximize the deposition characteristics of alumina films sputtered from a solid target in an  $\text{Ar}/\text{O}_2$  ambient. Semi-crystalline ( $\kappa+\theta$ ) alumina has been reported using a similar technique at temperatures as low 370 C. The difference in the system used herein is that RF power is used for

both, the inductive and capacitive components. Additionally, we use a solid target made of sintered alumina throughout the experiment.

A model is developed using regression analysis and compared to results obtained. Because plasma parameters can interact with each other, we explore ICP/CCP power interactions and gas influence on deposition. The design and analysis is done using RS/1, which is the industry standard for statistical analysis.

Results of this study indicate the ability to grow  $\text{Al}_2\text{O}_3$  at rates close to 200 Å/min. The samples analyzed via ESCA show a perfect match to the most common hydrated phases of alumina. XRD analysis indicates the films to be amorphous, but that is not unexpected given the low temperature at which the films were grown. Film properties are shown to be a function of the current density flux set up by the ICP source, and the ion energy to the target as determined by the CCP source

Patrick F. Gonzalez  
Electrical Engineering Department  
Colorado State University  
Fort Collins, CO 80523  
Spring 2000

## Acknowledgements

The author would like to thank his advisor, Dr. George Collins, for his guidance and flexibility in accommodating my special circumstances of full time employment. In addition, the author would like to acknowledge Dr. Derek Lile, Dr. Harry Edwards and Dr. Tom Chen for being part of the advisory and examination committee. The author would also like to thank all the students and supporting staff with whom he worked at ERC during the years 1992 through 1998.

The author would like express his gratitude to his mother Ernestina, father Patricio and brother Andy for their never-ending encouragement. Last but not least, the author would like thank his wife Anne Kristiina for her unconditional love and support during all phases of this endeavor, and to God for giving him the ability to complete this work.

## Autobiography

The author was born in Valparaiso, Chile in the Summer of 1966. He attended a private French school where he was considered a fairly good student and remained enrolled until the seventh grade. In 1978, he immigrated to the United States with his family and enrolled in the Dade County public school system.

In 1980, the author won a school-wide award for his achievements in the biological sciences. Two years later, he enrolled in the gifted program at Coral Gables High School that allowed him to work along side with scientists at the School of Marine of Science at the University of Miami. He graduated 11<sup>th</sup> out of 664 students and went on to study Physics at the University of Chicago upon graduation.

The author's pragmatic side was out of place with the classical education at the University of Chicago so he transferred to the University of Miami to finish his career in Electrical Engineering. In 1988, his application for Amnesty was finalized and became permanent resident of the United States. In 1989 he was awarded his BSEE. The author went on to obtain his MSEE from the University of Vermont where he studied applications of eCR systems under a grant from IBM, and graduated in 1991.

The author then enrolled at Colorado State University during the 1992 Spring Semester and finished his Ph.D. course work within a year. In 1993 he left school and accepted a position as a process engineer with NCR microelectronics, the same year he became a US citizen. In 1995 he won a company-wide quality award and was promoted to Principal

Engineer. He transferred to the plasma-processing group at NCR and re-enrolled at Colorado State University.

In 1997, the author left NCR/Symbios Logic and accepted a job as a hardware engineer in the manufacturing group at Hewlett-Packard. The same year, he agreed to serve as an outside advisor to the graduate board of the McNair program at Colorado State University.

In 1999, the author accepted a promotion to individual contributor at the imaging division of Hewlett-Packard in Greeley, where he is presently employed. He lives in Fort Collins with his wife Anne and enjoys outdoor winter sports.

Dedication

In Memory

of

Patricio Lisandro Gonzalez Villalon

August 15<sup>th</sup> 1941-May 23<sup>rd</sup> 1998

LXXXIX

*Cuando yo muera quiero tus manos en mis ojos:  
quiero la luz y el trigo de tus manos amadas pasar una vez mas sobre mi su frescura:  
sentir la suavidad que cambio mi destino.  
Quiero que vivas mientras que yo, dormido,  
te espero, quiero que tus oidos sigan oyendo el viento,  
que huelas el aroma del mar que amamos juntos y que sigas pisando la arena que pisamos.  
Quiero que lo que amo siga vivo y a ti te ame y cante sobre todas las cosas,  
por eso sigue tu floreciendo, florida,  
para que alcances todo lo que mi amor te ordena,  
para que se pasee mi sombra por tu pelo,  
para que asi conozcan la razón de mi canto.*

*Pablo Neruda*

## Table of Contents

Chapter 1 Introduction.....	1
1.1 Motivation Behind This Study.....	1
1.2 Why Inductive Plasmas.....	3
1.3 Potential Applications.....	8
1.4 Advantages Over Existing Techniques.....	11
1.5 Alternative Approaches.....	13
Chapter 2 Background Theory.....	16
2.1 Particle Distribution in a Plasma.....	16
2.2 Charge Particle Transport.....	23
2.3 Sheath Formation.....	29
2.4 Conclusion.....	31
Chapter 3 Modeling and Measuring Techniques.....	34
3.1 Transformer Formalism.....	34
3.2 Plasma Characterization Techniques.....	38
Chapter 4 Literature Review.....	44
4.1 Why RF.....	44
4.2 Properties of Alumina.....	49
4.3 Survey of Previous Studies.....	52
Chapter 5 First Configuration.....	56
5.1 Technical Approach.....	56
5.2 Analysis of Results.....	62
5.3 An alternative Approach.....	73
5.4 Conclusions.....	76
Chapter 6 Second Configuration.....	77
6.1 Changes Implemented.....	77
6.2 Analysis of Results.....	79
6.3 Composition Analysis.....	86
6.4 Microstructure Analysis.....	92
6.5 Conclusion.....	98
Chapter 7 Suggestions for Further Study.....	101
References.....	103
Appendix.....	108

## List of Figures

### Chapter 1

Figure 1.2.1. Inductively driven reactors in cylindrical and planar geometries, after Lieberman .....	7
Figure 1.2.2 Final configuration of alumina sputtering system .....	8
Figure 1.3.1 A typical magnetic writing head .....	10
Figure 1.4.1 A typical planar magnetron, after Chapman .....	12

### Chapter 3

Figure 3.1.1 Circuit Model for an inductive plasma .....	36
Figure 3.2.1 Typical Langmuir probe characteristics obtained with a cylindrical probe .....	40

### Chapter 4

Figure 4.1.1 The deposition rate of $AlO_x$ as a function of Reactive gas partial pressure after Sproul, et.al .....	46
Figure 4.1.1. Typical hysteresis loop in reactive sputtering of Alumina .....	47
Figure 4.2.2 Thornton's structure-zone model for sputtered films. $T$ is the substrate temperature and $T_m$ is the coating material melting point. ....	53

### Chapter 5

Figure 5.2.1 Deposition Rate vs CCP Power, 100% Ar ambient ....	68
Figure 5.2.2 Deposition Rate vs Pressure, 100% Ar ambient ....	69
Figure 5.2.3 Deposition Rate vs ICP Power, 100% Ar ambient ....	70
Figure 5.2.4 Contour plot of alumina dep rate .....	72
Figure 5.3.1 Deposition Rate vs ICP power for different CCP powers, pressure=10 mT .....	75
Figure 5.3.2 Deposition Rate vs ICP power for different CCP powers, Pressure=30 mT .....	75

### Chapter 6

Figure 6.2.1 Alumina sputtering rate (A/min) in 100% Ar, pressure at 15 mTorr .....	83
Figure 6.2.2 Alumina sputtering rate (A/min) in 98% Ar, and 2% $O_2$ , pressure at 15 mTorr .....	84
Figure 6.2.3 Alumina sputtering rate (A/min) in 96% Ar, and 4% $O_2$ , pressure at 15 mTorr .....	85
Figure 6.3.1 Film 1 compared to $Al_2O_3$ solid standard. Dep parameters are ICP=300, CCP=0, P=20mT, 100% Ar ambient .....	89

Figure 6.3.2 Film 3 vs Al <sub>2</sub> O <sub>3</sub> solid standard. Dep parameters are ICP=0, CCP=300, P=30mT, 100% Ar ambient.....	90
Figure 6.3.3 Film 6 vs Al <sub>2</sub> O <sub>3</sub> solid standard. Dep parameters are ICP=0, CCP=400, P=10mT, 100% Ar ambient.....	90
Figure 6.3.4 Film 16 vs Al <sub>2</sub> O <sub>3</sub> solid standard. Dep parameters are ICP=400, CCP=0, P=30mT, 100% Ar ambient.....	91
Figure 6.4.1 Counts vs 2θ for sample 35.....	95
Figure 6.4.2 Counts vs 2θ for sample 41.....	95
Figure 6.4.3 Counts vs 2θ for sample 44.....	96
Figure 6.4.4 Counts vs 2θ for sample 47.....	96
Figure 6.4.1 Counts vs 2θ for sample 59.....	97
Figure 6.4.1 Counts vs 2θ for plain quartz slide.....	97

## List of Tables

### Chapter 5

Table 5.2.1 Results of response surface experiment with power and pressure as variables and film thickness as response .....	63
Table 5.2.2 Properties of planar magnetron sputtered Al <sub>2</sub> O <sub>3</sub> films, from Nowicki .....	65
Table 5.2.3 Anova table from the first set of data, 100% Ar ...	67
Table 5.2.4 Summary of Parameter Estimates and model fit .....	70

### Chapter 6

Table 6.2.1 Sputtering Rate (A/min) in 100% Ar ambient, pressure at 15 mTorr .....	83
Table 6.2.2 Sputtering Rate (A/min) in 98% Ar and 2% O <sub>2</sub> ambient, pressure at 15 mTorr .....	84
Table 6.2.3 Sputtering Rate (A/min) in 96% Ar, and 4% O <sub>2</sub> ambient, pressure at 15 mTorr .....	85
Table 6.3.1 Percent composition obtained from ESCA on four Films and a Al <sub>2</sub> O <sub>3</sub> standard.....	87
Table 6.3.2 ESCA composition at. % after sputtering for 8 nm ..	88
Table 6.4.1 Aluminum Oxide, Monoclinic Standard ( $\theta$ ), $\lambda=1.54056$ .....	94

### Appendix

Table A1 Details of the runs for the second set of Experiments .....	108
Table A2. Langmuir probe measurement obtained on 100% Ar plasma.....	109

## CHAPTER 1. INTRODUCTION

### 1.1 Motivation Behind This Study

The basis for this study is essentially an extrapolation of the experiment first demonstrated by Yamashita and later refined by Rossnagel and Hopwood<sup>1</sup> on what they called Physical Vapor Deposition (PVD) of metals. Here, the researchers combined for the first time DC magnetron sputtering and inductive coupling in order to accomplish high rates of ionization and highly directional deposition of material. The technique was first demonstrated in 1989 to show how metal ions could be sputtered from a solid target and then ionized as they transversed a high density plasma region created by an inductive coil placed *inside* the chamber. The ionized metal could then be "accelerated" to the film by either grounding it or through a bias set up at the substrate. Deposition rates were shown to be equal or in some case larger than conventional DC magnetron sputtering.<sup>2</sup>

For this study, we modified Yamashita's concept and adapted it to the sputtering of ceramics from a solid target. In order to accomplish this task, we set up a high-density plasma by running a time varying current through several turns of a 4" Cu coil outside the chamber. The plasma was localized to a region between the magnetron cathode and the sample position. An RF source at 13.56 MHz was attached to the solid alumina target to set up a conventional capacitively coupled system to sputter off the material. At high pressures a large fraction of the alumina sputtered from the magnetron is ionized. In the ICP region, these ions are accelerated across the sheath of the grounded substrate holder and deposited at a normal incidence. Because the target is an insulator, there is also a large component of secondary electrons emitted. These secondary electrons

serve to enhance the surface mobility of the arriving species, thereby affecting the properties of the film. Ionization rates on the ICP region have been reported to be upwards of 85% in the ICP zone at pressures around 50mT. The plasma confined between the RF coils has an increased density due to the elevated electron temperature caused by the circular motion of the electric field. As the sputtered atoms pass through the dense plasma they are ionized by either electron impact ionization or Penning ionization. This high level of ionization is reputed to change the film properties as well as enhance the sputtering rates reported in this thesis.

It should be recognized that coatings deposited via sputtering are always found in the state of compressive stress. This stress is caused by the atomic bombardment of the film by energetic species in a process called "atom peening".<sup>3</sup> Moreover, the surface of the growing coating is also submitted to bombardment by neutral gas atoms, namely ions that are neutralized at the cathode and back-scattered with an energy of the same order of magnitude as that of the accelerated ions. These types of bombardment decrease in magnitude with increasing plasma pressure because of the decrease in mean free path of the sputtered target atoms and back-scattered gas atoms. The kinetic energy of these particles is also decreased as the power decreases.

Most applications described in literature using an ICP/CCP approach have been for sputtering of metals. Notably Schneider, *et.al.*<sup>4</sup> have refined PVD further with the application to reactive sputtering of  $Al_2O_3$  using pulsed DC power at the cathode. The idea is that DC sputtering can reportedly achieve sputtering rates close to that of metals, since the sheath potential is close to that of the net DC bias. Nevertheless, all the drawbacks inherent to reactive sputtering such as arcing and target poisoning are still present. Herein, we describe what we believe is the first application

of PVD to the sputtering of a solid alumina target at low temperatures using RF for powering the inductive coil and the cathode. More precisely, this thesis explores the technical challenges behind the implementation and the solutions to these issues:

- i. How the plasma parameters interact with each other?
- ii. How can we independently change plasma density and substrate bias to affect film characteristics?
- iii. How can we design a source that can be run for long enough to produce thick films?
- iv. Is the process robust and feasible for manufacturing implementation?

## **1.2 Why Inductive Plasmas**

A plasma can be defined as a partially ionized gas in which the charged species have a sufficient concentration such that they interact significantly through Coulombic interactions. The charged species within the plasma respond as to oppose any applied field and to maintain overall neutrality in the plasma. The Coulombic interactions give the plasma a fluid-like behavior, where the motion of charged species is coupled to the movement of the neighboring charged particles. Normally the plasma glow behaves like a fluid and the glow fills the region in between the electrodes and wets the surfaces in contact with the glow.

In plasma processes for the fabrication of microelectronics, DC or radio frequency (RF) glow discharges are used to etch or, as in this work, sputter material onto wafer surfaces. These plasmas can produce highly reactive neutrals and ions at low temperatures by the introduction of energy into the plasma through

its free electrons that in turn collide with the neutral gas molecules.

The type of plasma discharge continuously referred to in this thesis is a non-equilibrium plasma in which the electrons have a greater average energy than the ions and neutrals due primarily to differences in mass. A plasma is sustained by the introduction of energy from an electric or magnetic field. The electrons are accelerated by the field, thus gaining energy that is passed to the neutrals through collisions. The low rate of energy exchange is in the elastic collisions between the much heavier neutrals and the electrons result in the significantly higher average energy of the electrons. The electrons can, therefore, gain sufficient energy to produce (through inelastic collisions with neutral gas molecules) significant amounts of ions, free radicals, and other excited species without appreciably heating the gas thermally. Consequently, at room temperature, we effectively have a state where we have significant amounts of free radicals and ions at room temperature. Since the gas phase and surface reactions of free radicals and excited species have lowered activation energy, the kinetics can be greatly enhanced.

Plasmas are used in all major microelectronics processes: sputtering, plasma enhanced chemical vapor deposition (PECVD), and plasma etching. In each, the plasma is used as a source of ions and/or reactive neutrals, and is sustained in a reactor so as to control the flux of neutrals and ions to a surface through external means.

ICPs have been used and studied for over 100 years. However with the recent trend toward high throughput single wafer renewed interest in high-density plasmas has emerged. While most production systems as of today (1996) are capacitively coupled, inductive plasmas are becoming increasingly important due to several advantages over its predecessors. Although the knowledge base for ICP

has exploded during the recent years, there are still issues that are openly debated. One, for example, is about the true nature of the discharge, since inductive discharges have a capacitive component, which becomes stronger at low input powers.

In the sputtering system designed for this work, a ¼" Cu coil is wrapped several times around a quartz chamber. This creates a capacitive coupling to the plasma in addition to the inductive coupling, that is in fact, necessary to light the plasma. In some cases a significant sheath can be created such that it becomes necessary to minimize this effect to prevent sputtering from the coil. Indeed this is a topic of continued research, where significant contributions to the understanding of parasitic capacitive effects have come out of another group under the supervision of Collins, et.al.<sup>5</sup>

Methods most often used to reduce the parasitic capacitive coupling include inserting a conducting shield (Faraday shield) around the discharge chamber to short out the axial electric fields. Such a shield was originally part of the source used in this report, but later taken out when it was found that the films had very low impurities, an indication that sputtering from other sources other than the target was not occurring. Additionally, the plasma was very difficult to light with the shield in place.

One of the more attractive attributes of ICPs are the ability to operate at a higher plasma density ( $10^{17}$ - $10^{18}$  m<sup>-3</sup>) and low pressures (1 - 50 mTorr). The ICP is excited and sustained by passing radio frequency (RF) current through a coil adjacent to the plasma region. The RF magnetic flux generated by these currents penetrates into the adjacent discharge region. Using Faraday's Law,  $\nabla \times E = -\frac{\partial B}{\partial t}$ , one can see that the time varying rf magnetic flux density  $B$  induces

a solenoidal rf electric field  $E$ . It is this circular electric field that accelerates the electrons in the discharge and sustains the plasma. It is precisely these circular fields which cause circular currents which minimize the electron losses to the walls. In contrast, the  $E$  field in a capacitively coupled system is perpendicular to the substrate, causing increased electron losses and a less dense plasma.

Typically, a dielectric window made of glass or ceramic separates the plasma and coil. The most common materials are quartz ( $\text{SiO}_2$ ) and alumina ( $\text{Al}_2\text{O}_3$ ). Although the geometric variations are endless, figure 1.2.1 shows the two most common source geometries for ICPs.

As mentioned, ICPs create higher density plasmas, which in turn imply more collisions between molecules and decreased mean free path. Higher plasma densities also decrease the sheath thickness  $s_m$ , since it is roughly proportional to  $(1/n_s)^2$ . It should be obvious, then, that the ions will impinge on the substrate with less energy than in a purely capacitive system, leading to less film damage and reducing the chance of film re-sputtering. (The interested reader is referred to chapter 2 for further details on the Child-Langmuir equation, from which the relation between  $s_m$  and  $n_s$  is derived.) In turn, low pressure reduces the potential for contamination from gases onto the wafers and enhances the directionality of the ions.

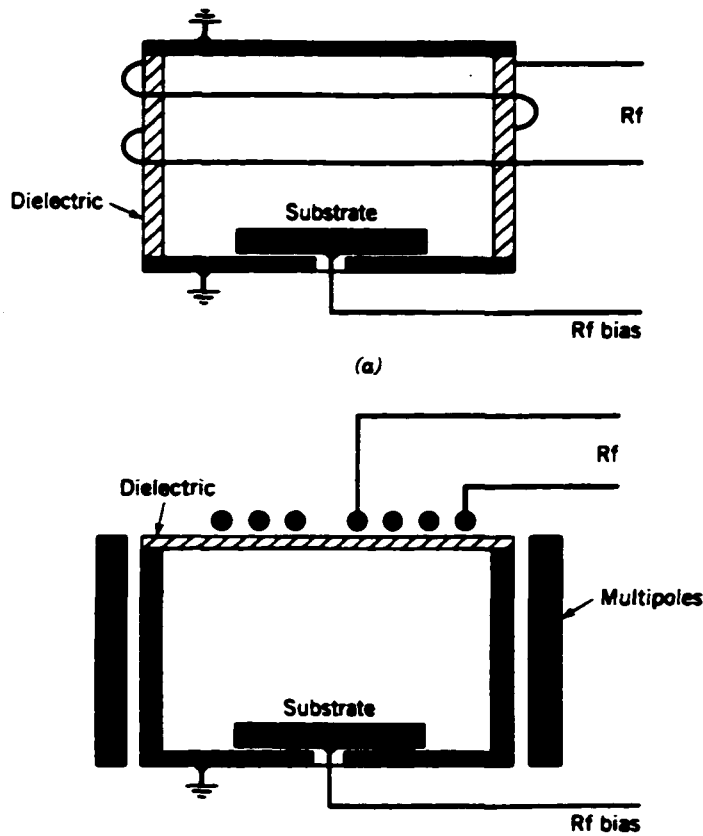


Figure 1.2.1 Inductively driven reactors in a) cylindrical and b) planar geometries from Lieberman<sup>6</sup>

Figure 1.2.2 demonstrates schematically the system designed to prove the ICP aided sputtering concept. The original intent was to develop a very compact source using the planar configuration. In practice, however, it was quite complicated to shield the inductive fields properly as to allow for individual adjustment of the power supplies. This is one of the reasons we adopted the alternative cylindrical configuration. The plasma is likewise cylindrical in shape. Due to the low-pressure regime in which this system is run, the plasma diffuses throughout the chamber so that it nearly homogeneous throughout, even though the conductive

plasma near the edges tends to shield the bulk plasma from the RF fields. The skin depth  $\delta$  for a 13.56 MHz inductive plasma is typically a few centimeters. Therefore, most of the electron heating takes place in the region close to the window through which the magnetic field is most intense.

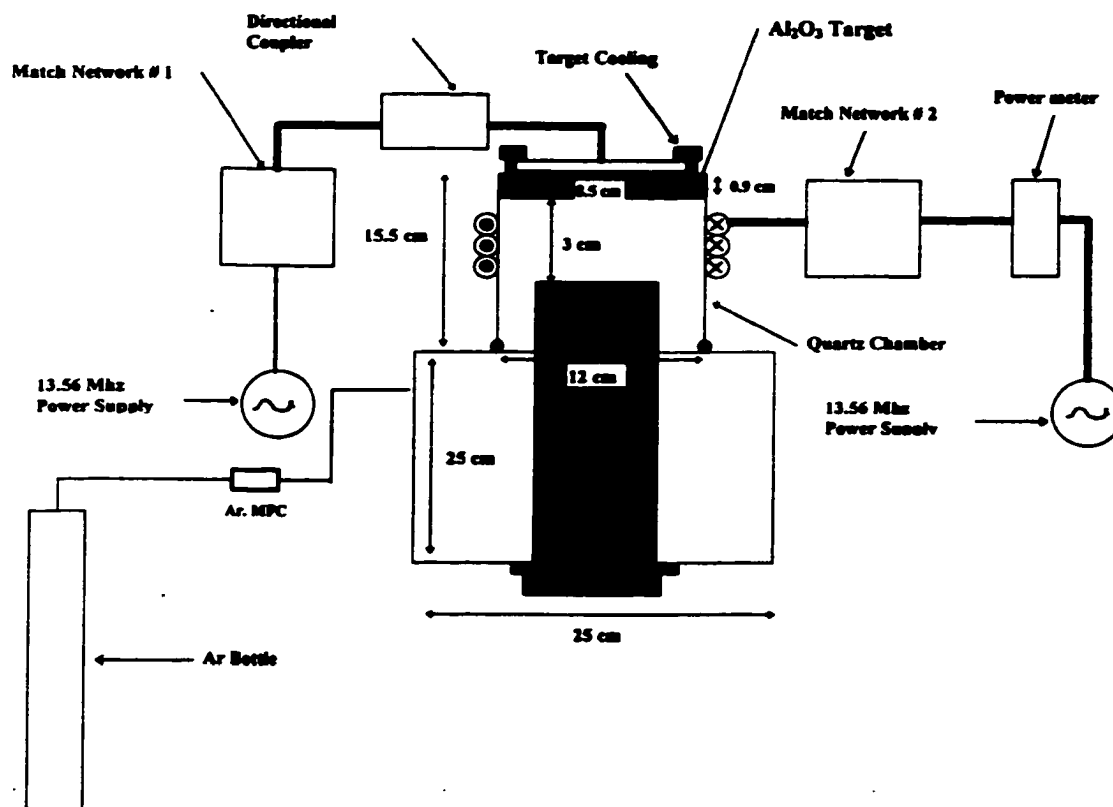


Figure 1.2.2 Final Configuration of Alumina Sputtering System.

### 1.3 Potential Applications

Applications for this technique are varied. Most notably ceramic coatings grown at low temperatures can be deposited onto polymers for packaging applications where high gas barrier properties

are needed. Key elements for such usage is a dense microstructure and a high rate of deposition. More importantly, the entire process must take place below the melting point for such polymers, which may be quite low. The reactor tested herein is capable of depositing thick amorphous alumina films at the low temperatures that may be required for deposition onto polymers or other substrates incapable of tolerating high temperatures.

Another very important application for this type of research is for magnetic head applications. The magnetic data storage industry is undergoing a trend of increasing recording density at a compound rate of about 60% year.<sup>7</sup> This requires, among other things, thinner insulating layers, so called gap layers, between the pole pieces, and between the shield in the case of a magneto-resistive (MR) head. Currently, gap-layer deposition is achieved through DC sputtering, where issues such as thickness and stoichiometry control are difficult to achieve.

Simplified sketches of a magnetic recording head are shown on figure 1.3.1. The view from the top of the writing head shows a spiral coil wrapped between two layers of magnetic material. We note that at the lower end there is a gap between these layers, and their upper end, these layers are joined together. The N-S poles at the gap end of the writing head concentrate the field to make this region the "working" end, which is the area where the writing fields leaks into the space outside the head. When a magnetic storage medium ( a spinning computer disk, for example) is put in close proximity with the writing head, the hard magnetic head material on the disk surface is permanently magnetized (written) with a polarity that matches the writing field.

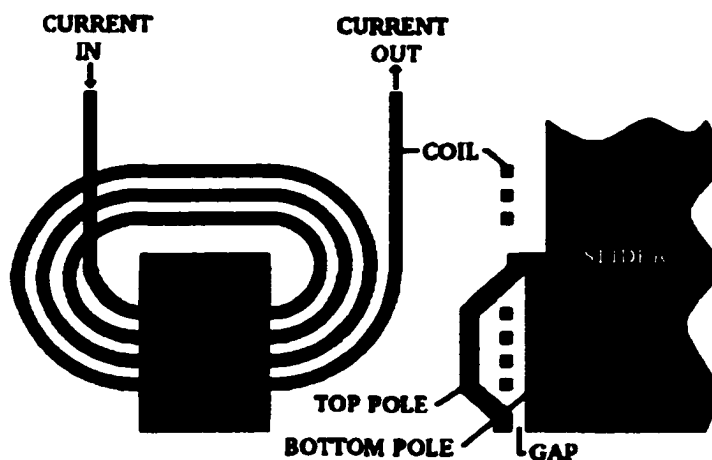


Figure 1.3.1 A typical magnetic writing head

The "gap" between the top and bottom poles of this magnetic head can be several microns thick and is normally filled with a dielectric such as  $\text{Al}_2\text{O}_3$ . Because of the thickness required and uniformity needed, deposition is normally done by reactive sputtering. However, issues such as thickness control and oxygen stoichiometry have been a challenge.<sup>4</sup> Additionally, film quality is of foremost importance, given that the recording heads fly very close to the surface of the magnetized disk. One is faced with the dilemma of producing film at a rate fast enough to make manufacturing viable while maintaining the proper physical characteristics of the desired films. The system tested herein attempts to fulfill this need as well.

Another application of alumina films in the near future is for replacement of silicon dioxide as gate dielectric. Good quality alumina films have a dielectric constant of around 12, or 12 times more electrical charge than air and approximately three times more than  $\text{SiO}_2$ . Armed with three times the electrical charge of silicon dioxide, alumina films might enable a factor of three

reduction in the size of transistors. This is particularly interesting, since SiO<sub>2</sub> technology will soon reach its limit. That's because as the thickness of a silicon dioxide dielectric becomes smaller, a quantum mechanical tunneling effects causes electrons to leak out and make the transistors less efficient. If thin alumina films carry three times the charge for the same thickness as silicon dioxide, it may be possible to make the alumina film three times thicker than it would be required for silicon dioxide and achieve the same results.

#### **1.4 Advantages Over Existing Techniques**

Because of the insulating properties of dielectrics, a time varying field is necessary for sputtering from a solid target. This is traditionally accomplished by coupling RF power to the target. Normally, a noble gas such as Ar is added to the chamber whereby the ionized gas mechanically causes the release of material from the target. The electric field that attracts the ions towards the target also repels the electrons from the target into the plasma. In this configuration, *the ion density and ion energy are thus effectively coupled*. The discharge created by the application of this time varying field creates both ions and electrons. Electrons, however, are rapidly lost to wall recombination due to their higher mobility. If reducing losses to the walls could enhance the lifetime of these electrons, then the plasma intensity may be enhanced. This has given rise to the so-called magnetron systems.

Here a static magnetic field is superimposed over the target. The electrons will tend to follow the paths of the magnetic flux lines, so that one is effectively increasing their path length as shown on figure 1.4.1. Magnetrons have been shown greatly increase the deposition rate of [metallic] materials by increasing the

ionization rate.<sup>9</sup> The superposition of a magnetic field over can help to increase the plasma density. However, this is not often enough to significantly raise the sputtering rate in dielectric material such as  $Al_2O_3$ . Even worse, magnetrons can have undesired secondary effect of causing uneven erosion of the target material.<sup>10</sup>

Clearly, there should be a better way to increase the plasma density and hence the sputtering rates of dielectrics so that one can achieve rates comparable to metals and possibly eliminate secondary effects of uneven wear of the target. Such a result can be achieved rather simply by inductively setting the plasma density and capacitively sputtering material. Additionally, the "dynamic" magnetic field set up by the inductive coil also has the advantageous effect of preventing localized erosion of the target. From the manufacturing standpoint, we obtain the additional benefit of lengthening the life of the target and ultimately save on cost.

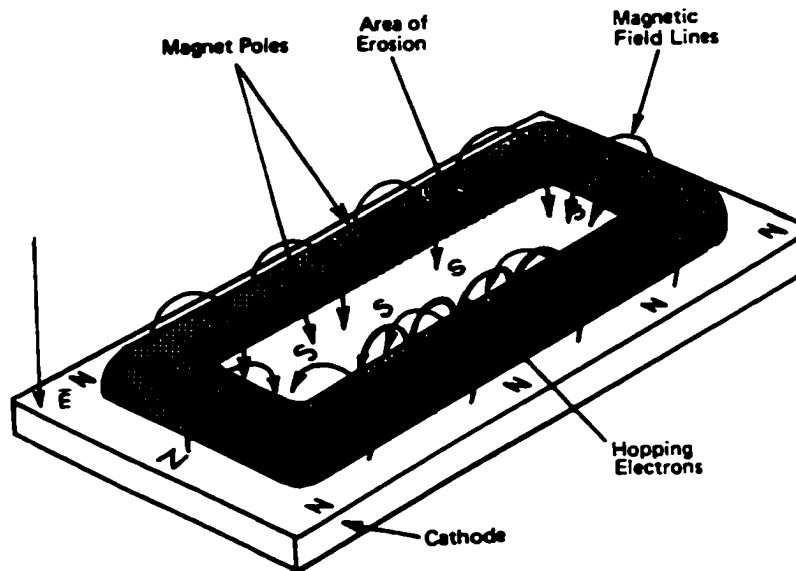


Figure 1.4.1 A Typical Planar Magnetron from Chapman.<sup>11</sup>

In PVD, one sputters atoms into an inductively coupled plasma (ICP) region, producing high ionization fractions. The atoms are ionized in the high-density plasma, where they eventually fall across a thin sheath that appears across the substrate. (Note that due to the varying degree of mobility between the ions and the electrons, there will always be a sheath formed as to reduce the loss of electrons.)

If the chamber is at low enough pressures, then these ions fall across the sheath in a highly collimated fashion. The energy of the ions impinging on the surface then can be controlled by applied bias to the substrate if necessary. By monitoring and controlling the intensity of the ion bombardment, the physical characteristics of the film can be altered. In this study, we set the bias on the substrate bias to zero by directly connecting it to ground. Based on our plasma potential measurements by Langmuir probe technique, we find the sheath potential on the order of 40 V to 50 V. This is sufficient enough to assure directionality without running the risk of inducing material re-sputtering from the sample.

### **1.5 Alternative Approaches**

For the deposition of thin films, magnetron sputtering is extensively used because of its high rate, ease of use and quality of the deposited films. Recently, researchers have taken this original idea and added the functionality of ICP, demonstrating applications to the deposition of alumina thin films with good results.<sup>12</sup> By modifying the magnetron from straight DC to pulsed DC power, they were able to achieve: 1) high deposition rates ( 76 % of metal deposition rate) 2) polycrystalline material at relatively low substrate temperatures (  $T < 500$ ) and 3) densities and hardness comparable to the sapphire standard. Schneider's innovative approach

is an encouraging advancement for potential applications that can take advantage of this technology, namely magnetic read-write heads<sup>13</sup>, diffusion barriers for semiconductor applications<sup>14</sup>, corrosion resistant coatings<sup>15</sup>, and food packing<sup>16</sup>.

Yamashita was one of the first ones to exploit the benefits of plasma densification when he immersed a helical coil inside a chamber with a metal target DC biased at one end.<sup>17</sup> Rossnagel, et. al. Realized the utility of this approach and sought to combine it with DC sputtering of solid metals to create a flux of ionized species that could fill damascene structures.<sup>18</sup> Schneider, et. al. changed the approach to sputtering by implementing pulsed DC in an effort to reactively sputter alumina from a solid Al target in an O<sub>2</sub> ambient.<sup>19</sup> In this thesis we refine the approach to sputtering alumina by implementing two important changes:

- i. sputtering from a solid alumina target with Ar instead of reactively making alumina and,
- ii. using RF magnetron sputtering instead of DC.

Judging from the efforts and interest on inductive plasma processing, there is a continued need for improvements that yield simple and more robust processes. The study presented herein attempts to do just that by building on the proven concept of ICP/CCP combination and simplifying the current sputtering techniques.

Traditional arguments against sputtering from a solid alumina target have been the historically low rates and the manufacturing difficulties arising from having to use large power densities. Nevertheless, we show that by taking a few precautions, namely proper cooling and shielding, we can achieve decent sputtering rates of alumina films with nearly perfect

stoichiometric. Additionally, by utilizing response surface methods, we gain further insight into the interaction between the plasma parameters that maximize the growth rate.

## CHAPTER 2 BACKGROUND THEORY

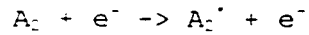
A general idea of the theory is always helpful to understand the effects that are at work in this thesis. Consequently, this chapter will describe the development of key equations from some very basic concepts. We do not show explicitly the derivation, but rather give references for the reader who is interested on the details that are left out. The principal aim is to explain the effects of variations on the plasma that lead to the properties sought after for the deposition of thin films.

The important notions for understanding a plasma discharge are reviewed from basic principles. The development follows closely to the self-consistent approach developed by Lieberman and Lichtenberg on their book about plasma discharges.<sup>20</sup> Because the plasma system is dynamic in nature, we choose to look at the global picture when necessary, and therefore, apply average values to look at *macroscopic picture*. The inter-particle collisions are considered independently of the larger scale fields to determine an *equilibrium distribution*.

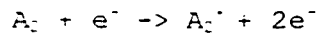
### 2.1 Particle Distributions in a Plasma

The experiments described herein deal with partially ionized gases that are composed of ions, electrons and neutral species. The electrons undergo collisions with neutrals, producing excited species, free radicals, ions and additional electrons. The typical reactions that take place in the plasma as a result of electron collisions are:

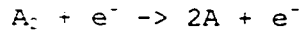
i. Excitation: (rotational, vibrational)



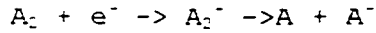
ii. Ionization



iii. Dissociation



iv. Dissociative Attachment



Dissociative processes usually have a lower threshold than ionization processes.

In our experiments, the plasma-state is created by the introduction of energy through electric fields as in the capacitive case or magnetic fields, as in the inductive case. The electrons, which couple the fields to sustain the plasma, lose their energy to the neutrals through any of the processes mentioned above. The rate of energy transfer in these elastic collisions is low due to the electron mass being much less than that of the neutrals. Because the density of the particles is low and the fields are strong, the electrons lose energy too slowly to be in equilibrium with the neutrals. In the experiments to be described here, typical values for the glow discharge are as follows: Plasma density of  $10^8$  to  $10^{12}$  per  $\text{cm}^3$ , ionization 0.1 %, average electron energies of 1 to 10 eV, and average neutral or ion energy of  $3/2$  kT or about  $1/25$  of an eV.

The electron-velocity distribution plays an important role in determining the properties of the plasma. Once we know it, the transport properties of the ions can be derived. As suspected, the electron-velocity distribution is a function of the strength of the field that sustains the plasma as well as the concentration of neutral and charged species within the plasma. The electron velocity distribution function  $f(r, v)$  represents the concentration of

electrons at a particular point in space,  $\mathbf{r}$ , that have a velocity vector  $\mathbf{v}$ , so that the concentration of electrons is simply the integral of the distribution function over all space:

$$n = \iiint_{\mathbf{r}} f d\mathbf{v} \quad 2.1.1$$

The particle flux is then simply  $n \langle u \rangle$ , where  $u(\mathbf{r}, t)$  is the mean velocity. The exact form of the electron-velocity distribution can be derived from the Boltzman transport equation, which is an electron energy balance over a differential element of real and velocity space. We present here the general form taken from Lieberman's book:

$$\frac{\partial f}{\partial t} + \mathbf{v} \cdot \nabla_{\mathbf{r}} f + \frac{eE}{m} \cdot \nabla_{\mathbf{v}} f = \left. \frac{\partial f}{\partial t} \right|_{\text{coll}} \quad 2.1.2$$

The first term represents the change in the number of electrons within a volume that have a certain velocity. The second term represents the net number of electrons lost or gained by movement of electrons in or out of our differential volume. The third term is indicative of the change in the number of electrons at a given energy due to their acceleration by the electric field. In addition to the flows in or out of our differential volume, we can have very rapid appearance or disappearance of electrons due to collisions with other particles in a time scale shorter than the evolution of  $f(\mathbf{r}, \mathbf{v})$ . These are represented by the term on the right hand side of the equation. Holt and Haskel present a more rigorous derivation of the Boltzman equation 2.1.2, and the interested reader is referred to it.<sup>22</sup>

The function  $f(r, v)$  can be broken into isotropic and anisotropic terms. The isotropic term represents all the electrons that have a random direction and velocity distribution, but do not follow the electric field. The anisotropic term represents those electrons that have a favored direction caused by the electric field or concentration gradient. To solve for the electron distribution function, one normally assumes that the function  $f(r, v)$  can be represented as a linear sum of the isotropic  $f^0$  and anisotropic terms  $f'$ , so that  $f(r, v) = f^0 + \frac{v_z}{v} f'$ .

Substituting the expanded form of the electron velocity function back into the Boltzman equation and simplifying, one obtains:

$$\frac{\partial f^0}{\partial t} + \frac{v}{3} \nabla_r f' - \frac{eE}{3mv^2} \frac{\partial(v^2 f')}{\partial v} = \frac{\partial f^0}{\partial t} \Big|_{coll} = 0 \quad 2.1.4$$

and

$$\frac{\partial f'}{\partial t} + v \nabla_r f^0 - \frac{eE}{m} \frac{\partial f'}{\partial v} = \frac{\partial f'}{\partial t} \Big|_{coll} \quad 2.1.5$$

We note here an important point. Equation 2.1.4 gives the time rate of change of the isotropic part of the distribution given the anisotropic part. We set it equal to zero in the limit that the anisotropy is small. This equation would be used to find the electron energy distribution in the absence of spatial gradients or electric fields. It may be used to find the distributions at a certain temperature when the electrons and neutrals have reached equilibrium. However, this is rarely the case in gas discharges.

Equation 2.1.5 is to find the anisotropic portion of the distribution given the isotropic part. This would be used to find the electron distribution in an rf field. Many of the plasma characteristics at low pressure are derived from here. The collisional term on the right side of the equation represents the Coulombic, elastic and inelastic collisional loss terms. The Coulombic term is significant only at very high plasma densities found on nuclear fusion or perhaps high-density plasmas found on helicon or eCR systems.

Coulombic interactions become important when the ionization is perhaps on the order of 1%. The elastic collisions between the electrons and the neutrals lead to general heating but little exchange of energy due to the differences in the masses. They account for a significant randomization of the electron velocity distribution and greatly reduce the anisotropic nature of the electron velocity distribution. The inelastic collisions account for very little of the transport properties of the electrons. However, they do have a major effect on the distribution of velocities of the electrons and most importantly, on the physical and chemical properties of the plasma. It is the inelastic collisions that are responsible for the generation of ionized and excited species.

Suppose a sinusoidal electric field is imposed on a homogeneous plasma in the form of  $E(t) = \text{Re } E_0 e^{j\omega t}$ . Consequently the anisotropic term of equation 2.1.5 in the distribution function becomes:

$$f' = \frac{eE}{m(\mathbf{v}_m + i\omega)} \frac{\partial f^0}{\partial \mathbf{v}} \quad 2.1.6$$

where  $\omega$  is the frequency of the field,  $\nu_m$  is the elastic collision frequency for electrons and  $i$  is  $\sqrt{-1}$ . Additionally, we point out that the isotropic term may be considered time invariant for frequencies greater than the relaxation time of the electron energy by elastic collisions.

When calculating the collisional kinetics of a plasma used in microelectronics fabrication, only the isotropic distribution  $f^0$  is considered. Since the elastic collisions of electrons with neutrals are very frequent, they sufficiently randomize the field-induced directionality of the electrons, so that the anisotropic term can be neglected.

If we take the electric field to be low in the plasma, few electrons will suffer inelastic collisions, since the energy transition for inelastic excitation processes will exceed the energy of most electrons. Taking these assumptions, we substitute 2.1.6 into 2.1.4 to obtain after considerable simplification:

$$\frac{\partial f^0}{\partial v} \left[ \frac{e^2 E_0^2 M}{3m^2 \nu_m^2} + k_B T_g \right] + m v f^0 = 0 \quad 2.1.7$$

which has a solution:

$$f^0 = C \exp \left[ - \int_0^v \frac{m v dv}{k_B T_g + e^2 E_0^2 M / 3m^2 \nu_m^2} \right] \quad 2.1.8$$

For the case where the elastic collision cross section varies approximately as the reciprocal of the electron velocity (which is most of the cases),  $\nu_m$  is independent of the electron velocity. In

this case, equation 2.1.8 reduces to the well-known Maxwell-Boltzman distribution:

$$f^0 = C e^{-\frac{mv^2}{2k_B T_e}} \quad 2.1.9$$

$$\text{with } k_B T_e = \frac{e^2 E_0^2 M}{6m^2 v_m^2} \propto \left(\frac{E}{P}\right)^2$$

Here we have implicitly stated that the collision frequency  $\nu_m$  is proportional to the density of the gas particles with which the electrons collide and is proportional to the pressure. The electron energy is therefore a function of the electric field to pressure ratio  $\frac{E}{P}$ .

If the collision cross-section is assumed to be independent of the electron velocity (acting as hard spheres like He and H<sub>2</sub>), the distribution is called Druyvesteyn, and has the form:

$$f^0 = C \exp \left[ - \frac{\left(\frac{mv^2}{2}\right)^2}{e^2 E_0^2 M / 6mN^2 \sigma_m} \right] \quad 2.1.10$$

We note that the  $mv^2/2$  factor now has a square dependence and the  $E/p$  factor still remains. This distribution is more applicable to conditions where the  $E/p$  is high and the collision cross-sections are independent of electron energy.

For the Maxwellian distribution, the high-energy tail decreases as the exponential to the negative second power of the electron velocity, while the Druyvesteyn distribution declines as the

exponential to the negative fourth power. Thus the Druyvesteyn distribution predicts fewer high-energy electrons that can produce ions upon collisions. As the ionization increases, as one would expect with an ICP, the distribution becomes more Maxwellian. This is a result of the increased electron-electron scattering making the energy exchange within the electron population rapid, reducing the importance of the accelerating fields on the electrons.

## 2.2 Charge Particle Transport

Equation 2.1.1 describes the concentration of electrons in a finite volume. From here, the conductivity  $\sigma$  of the plasma can be derived from the flux of electrons that occurs when an electric field is imposed upon the plasma. This is of interest, since we gain an insight into the transport properties of the electrons within the plasma. The flux vector  $\Gamma$  is calculated from the electron distribution such that  $\Gamma = n \langle v \rangle = \iiint_{-\infty}^{\infty} v f dv$ .

We recall that the response of the electrons to an applied electric affects only the anisotropic term of the distribution. We refer back to equation 2.1.6, which we obtained by imposing an electric field to obtain:

$$J = -e\Gamma = -\frac{4\pi e^2}{3m} E \int_0^{\infty} \frac{v^3}{(v_m - i\omega)} \frac{\partial f^0}{\partial v} dv = \sigma E \quad 2.2.1$$

using the definition of the conductivity to be  $J = \sigma E$ . We assume that the primary charge carriers of the plasma are the electrons and that the ions do not appreciable contribute. This assumption is a

fairly good one, since at 13.56 MHz, the more massive ions gain little energy before the field reverses.

Simplifying the above equation for the conductivity, one obtains:

$$\sigma_i = \frac{\omega n e^2}{m(\omega^2 + \nu_m^2)} \quad 2.2.2$$

$$\sigma_r = \frac{\nu_m n e^2}{m(\omega^2 + \nu_m^2)} \quad 2.2.3$$

The real component relates the electric field strength to the current density that is in phase with the electric field. The imaginary component relates the component of the current density that lags behind the electric field, with a 90-degree phase shift. Under typical plasma conditions, the imaginary component of the conductivity is small, since the electrons suffer very frequent collisions with the neutrals with respect to the field frequency, so that the energy gained by the electrons from the field is rapidly randomized into isotropic electron energy. Under very low pressures, the plasma tends to store energy by accelerating and decelerating electrons, thus acting similarly to an electrical inductor. In practicality, since the resistivity is just the inverse of the conductivity, what we are really saying is that almost all of the rf voltage is dropped across the sheath regions and very little across the bulk of the plasma.

A net flux of electrons also results from spatial concentration gradients of electrons within the plasma. The calculation of the flux need only consider the anisotropic term of the distribution function that represents the spatial concentration,

since the isotropic portion cancels itself out. To accomplish this we solve equation 2.1.5 considering a steady state condition with a non-zero density gradient and DC electric field. What one obtains is the anisotropic term consisting of the product of the mean free path and the concentration gradient:

$$f' = \frac{v}{v_m} \nabla_r f^0 \quad 2.2.4$$

The total flux of electrons is then the result of the integration of the anisotropic term over all velocity space, which by definition, must be equal to the product of the diffusivity and the concentration gradient:

$$\Gamma = -\frac{4\pi}{3} \frac{1}{n} \nabla_r n \int_0^\infty \frac{v^4}{v_m} f^0 dv = -D \nabla_r n \quad 2.2.5$$

so that with simple algebra, the diffusivity becomes:

$$D = \frac{4\pi}{3} \frac{1}{n} \int_0^\infty \frac{v^4}{v_m} f^0 dv \quad 2.2.6$$

For a Maxwellian distribution with an elastic collision frequency that is independent of the electron speed, this reduces to :

$$D = \frac{k_B T_e}{m v_m} \quad 2.2.7$$

We also point out that the diffusivity  $D$  given by 2.2.7 is related to the mobility  $\mu$  by the Einstein relation  $\mu = \frac{|q|}{kT} D$

At this point it is important to review a few important concepts. The energy that sustains a glow discharge is transferred primarily via the free electrons within the plasma. It is then dissipated by collisions between the electrons and the other particles. Ultimately, it is converted into heating, excitation and dissociation of the gas as well as into photon emission from the plasma. The average power transfer from the electric field to a plasma is much like Ohm's law, where the real part of the conductivity  $\sigma_r$  is divided by the square of the electric field averaged over the entire cycle.

The concentration of charged particles in a typical plasma process is not constant, because the charge carriers recombine at any surface in contact with the plasma. The recombination or neutralization is very rapid and take place with nearly unity probability for charged particles striking a surface. The concentration of charged carriers, therefore, must approach zero as the surface is approached. In weakly ionized plasmas, which is the case throughout this thesis, the Coulombic interactions between the charges can be ignored and we can write an equation so that the diffusive and creative elements balance each other. This is generally reduced to solving the diffusion equation  $\nabla \cdot \Gamma = n_e \nu_i$  which says that the diffusive element must be equal to the creative element (ionizing collisions), and  $\Gamma$  is given by 2.2.5. The diffusion equation simplifies to:

$$D_e \nabla^2 n_e + n_e \nu_i = 0 \quad 2.3.1$$

For any given reactor shape, the concentration of charged species in a plasma can be calculated using the boundary conditions that the concentrations must be zero at a surface. In other words, the charged species are rapidly neutralized on collision with the surface.

The solution for the above equation is well known. Considering the one-dimensional case with the chamber length  $L$  for example, equation 2.3.1 takes the form of:

$$-D_e \frac{d^2 n}{dx^2} = n_e v_i \quad 2.3.2$$

with the boundary condition that  $n(0) = n(L) = 0$ . The fundamental solution of the above equation is:

$$n(x) = n_0 \sin(\beta x) \quad 2.3.3$$

with  $n_0$  the center density and  $\beta = \frac{v_i}{D_e} = \left(\frac{\pi}{L}\right)^2 = \frac{1}{\Lambda^2}$ . The

characteristic diffusion length  $\Lambda$  is a term that is used to compare the relative rate of diffusion losses among systems with different geometries.

At this point, let us briefly note that the boundary conditions that  $n(0) = n(L) = 0$  are not self consistent since they lead

to an infinite velocity at the edges, since  $u(x) = \frac{\Gamma}{n(x)}$ . This is due

to the fact that near the walls, the plasma quasi-neutrality of  $n_e \sim n_i$  does not hold. On the other hand, near the walls the electron density is much lower than the ion density, since the electrons have a higher mobility and they are depleted at a higher rate as they hit the wall surfaces. (This is the region we call the *sheath*, and shall be explored in greater detail later on.)

Since the bulk of the plasma is neutral in charge, an equal number of electrons and positive ions are created in the plasma. This means that the net surface flux for a steady state discharge in a container must be neutral or  $D_i n_i = D_e n_e$ . This does not mean that the concentration of charges species must necessarily be equal, just the flux coming into the plasma must equal the flux exiting the plasma.

When the Debye length (the distance at which a plasma can have a charge imbalance, or the distance at which the plasma appears to be uniform gas of neutral charge) is greater than the characteristic diffusion length  $\Lambda$ , a space charge  $E_{sc}$  can be created. This imbalance of charge dominates the characteristics of these lone charges such as their diffusivities. In order to keep neutrality, the net charge must be zero. Discharges used throughout this thesis normally meet this criterion, except in the sheath region where the plasma contacts the surface. Under these conditions, the fluxes caused by the diffuse elements must be equal to the field driven diffusion, so that we have:

$$\mu_i n_i E_{sc} - D_i \nabla n_i = -D_e \nabla n_e - n_e \mu_e E_{sc} \quad 2.3.4$$

Solving for the electric field  $E_{sc}$ , one obtains

$$E = \frac{D_i - D_e}{\mu_i + \mu_e} \frac{\nabla n}{n} \quad 2.3.5$$

Using the above expression for the electric field and recalling that  $\Gamma = nu = \pm \mu n E - D \nabla n$ , the one obtains after some manipulation the

result that  $\Gamma = -D_a \nabla n$  where  $D_a$  is called the ambipolar diffusion given by  $D_a = \frac{\mu_i D_e + \mu_e D_i}{\mu_i + \mu_e}$ .

In weakly ionized plasmas, which is the case throughout this thesis, the electron mobility is much larger than the ion mobility, therefore the ambipolar diffusion coefficient can be simplified to

$$D_a \approx D_i + \frac{\mu_i}{\mu_e} D_e = D_i + \frac{T_e}{T_i} D_i \quad 2.3.6$$

We can safely assume that in weakly ionized plasmas, the ions are in thermal equilibrium with the neutral gas and their temperature is of the order of the room temperature. However the electrons are far from equilibrium and their temperatures ranges from 1 to 5 eV so that we can simplify the above equation even further so that  $D_a \approx \frac{T_e}{T_i} D_i$

## 2.4 Sheath Formation

When the plasma comes in contact with a surface, it is perturbed and forms a sheath that is often very visible due to the plasma brightness. In an homogeneous plasma, a charged particle moves relatively freely. However, in the sheath region, the charge carrier density drops to the point that the assumption of neutrality is no longer valid and an electric-field forms to prevent the electrons from leaving.

The Child-Langmuir law describes this space charge region. The assumptions inherent in this equation is that the sheath is collisionless and all the ions enter the sheath with a pre-defined velocity which we call the Bohm velocity

Bohm proposed that there should be quasi-neutral transition region rather than an abrupt change from the bulk plasma to a space charge region. This was based on empirical measurements that indicated that the net ion current flowing to a non-floating object (e.g. cathode) was considerably greater than it was predicted by the model which had the sheath and bulk plasma joining at a discrete plane:

$$u(0) = \left( \frac{kT_e}{m_e} \right)^{1/2} \quad 2.4.1$$

This equation indicated the speed that the ion attains upon entering the sheath. Interestingly enough, the ion speed is dependent on the electron temperature  $T_e$ !

When a potential is seen by a plasma, the electrons in the sheath move to oppose the applied electric field, causing an imbalance of charged species in the sheath. This imbalance is known as a space charge  $\rho$ . The electric field can be calculated using Poisson's equation:

$$\frac{d^2V}{dx^2} = -\frac{\rho}{\epsilon_0} = -\frac{e}{\epsilon_0} (n(x)) \quad 2.4.2$$

Using conservation of energy, we likewise obtain:

$$1/2mv^2 = eV \quad 2.4.3$$

where  $V$  is the potential. We can substitute the above equation into 2.4.2 to obtain:

$$\frac{d^2V}{dx^2} = \frac{J}{\epsilon_0} \left( \frac{m}{2e} \right)^{1/2} \frac{1}{V} \quad 2.4.4$$

where we have used the fact that the current density  $J = nqv$  and the  $q=e$  for this case. To solve this equation we multiply this equation on both sides by  $\frac{dV}{dx}$  and then perform the integration with respect to the direction traveled to obtain:

$$j = \frac{4}{9} \epsilon_0 \left( \frac{2e}{m} \right)^{3/2} \frac{V^{3/2}}{x^2} \quad 2.4.5$$

## 2.5 Conclusion

The treatment of plasmas that has been shown in this chapter is sufficient for the understanding of most phenomena in semiconductor plasma physics. As we have seen, a plasma can be thought of having an isotropic and an anisotropic part. We equated the anisotropic part to an electric field to derive the electron distributions. We then took the anisotropic term for one of these distributions and determined the conductivity and diffusivity of the plasma. We then equated the diffusivity portion with the ionizing collisions through the diffusion equation to determine the density profile and sheath velocity. We then used the sheath velocity and Poisson's equation to derive the Child-Langmuir equation. It is this equation which describes the electrical properties of the plasma. Because we are combining two sources of RF power to independently tweak the density and energy of the ions, it is important to understand the parameters that govern the effects seen in this study.

In this thesis we also use an inductive source to set the plasma density which significantly complicates the plasma dynamics involved. Recalling that the coil is wrapped around the cylindrical chamber, there is a small sheath produced in front of the quartz. In inductive discharges, the sheath is generally in the order of a few

Debye lengths and the sheath voltage on the order of a couple of volts.

In order to fully describe the plasma, one must overcome significant mathematical hurdles, which have no closed form solutions. In most cases, the solutions can only be found through numerical methods. Although this is beyond the scope of this thesis, at least a general overview is presented since it is germane to the topic of discussion.

To begin with, the Child-Langmuir approximation is time-averaged model based on space charge limited ion current in the DC sheaths. A more accurate model that takes into consideration the inductive coupling is a dynamic RF sheath model for an arbitrary sheath voltage and collisionality of Godyak and Sternberg<sup>22 23</sup>

We have already explained the basics of an RF sheath through the development of the Child-Langmuir law. This theory is used to describe the space charge limited dc ion current to an electrode (grounded or negatively biased). This approach is applicable when the dc sheath voltage is much larger than the electron temperature  $T_e$  that controls the ion velocity at the plasma-sheath edge. We also assume collisionless ion motion and initial ion velocity equal to the Bohm velocity already given. In using the Child-Langmuir theory, we neglect the oscillating motion of the plasma-sheath interface. However, since ions essentially respond to the averaged dc component, a reasonable argument can be made for applying this model

Comparing the results with the more sophisticated GS (Godyak-Sternberg), one can be expected to obtain a sheath value 11% larger for a collisionless case (low pressure) and 15% smaller for the collision-dominated case. (high pressure). These are not exceedingly different values, but it is worth mentioning for completeness. Additionally, the disagreements become more pronounced

for small RF sheath voltages due to the existence of a residual dc sheath voltage as  $\frac{V_{sh}}{T_e} \rightarrow 0$ .<sup>24</sup> As a matter of fact, for small RF voltages,  $V_{dc}$  approaches the floating potential which is typically 12 to 15 V. This directly contradicts the wide spread assumption that the dc sheath voltage is proportional to the RF sheath voltage.<sup>25</sup>

## Chapter 3 MODELING AND MEASURING TECHNIQUES

In this chapter we describe the transformer model for inductive plasma. The model serves as an easy way to relate complex plasma parameters to a graspable circuit, which explains most phenomena that takes place in our reactor during processing. Additionally, we present a brief background on measurement techniques, which we use to characterize the film properties and the plasma characteristics.

### 3.1 Transformer Formalism

Attempts to model the inductive coupling between the coil and the plasma are numerous. Some of the first attempts date back to the 1930's.<sup>6</sup> The main idea has been to consider low-pressure inductive rf discharge as a secondary of an air core transformer. Such an approach is still widely accepted and provides good information about the discharge behavior.

Inductively coupled RF discharges can provide high-density plasma with low ion bombarding energy. In an inductive discharge, the plasma is created by applying rf power to a copper coil, resulting in the breakdown of the process gas within or near the coil by the induced electric field. In this study we used a two-turn coil which can be represented as the primary windings of an air core transformer. The plasma can then be considered as the secondary windings of the transformer. Using this formalism, one can derive some simple and useful relationships between the impedance characteristics and the physical properties of the plasma.

If we assume the transformer formalism stated above, then primary coil has an inductance  $L_1$  ( $X_m + X_1$ ), and a resistance  $R_1$ . The

secondary discharge inductance can be considered to have three components, a geometric inductance, an inertia inductance and a plasma resistance. The electrical properties of the plasma are described by the plasma conductivity as previously stated from equations 2.2.2 and 2.2.3. Considering the case where the collision frequency is much larger than the applied rf frequency, one obtains from 2.2.3 what we call  $\sigma_{dc}$  that signifies the plasma resistance and is simply  $\sigma_{DC} = \frac{e^2 n}{m v_m}$ . This value is representative of the plasma resistance that appears on the secondary of the transformer model as  $R_p$ .

Two inductive elements must be taken into account on the plasma for the transformer model. But first, we must consider the premise that the plasma forms current path that surrounds the primary coil and can be considered as a secondary of an air core transformer. Since the primary coil is surrounded by a conductive fluid (the plasma) and makes a closed electrical path about the primary coil, the premise of a secondary winding appears entirely reasonable.<sup>27</sup> The result is that the geometric inductance  $L_2$  can be deduced from classical transformer theory. A good approximation has been put forth by Piejak, et.al as  $L_2 = L_0 \frac{r^2}{r_0^2} \frac{1}{n^2}$  where  $r^2$  is the radius of the discharge path,  $r_0$  the radius of the primary coil and  $n$  is the number of turns.

The inertia inductance element is harder to define and essentially comes out of the imaginary component of the plasma conductivity as expressed by 2.2.2. We can consider the imaginary part of the plasma to be either a conductor with a conductivity  $\sigma_i$  or a dielectric with permitivity  $\epsilon_i$ . If we consider the permitivity instead, we find that at frequencies where  $\omega < \omega_{pe}$  (the plasma

frequency), which is true of most discharges,  $\epsilon_i < 0$ . A slab of such a plasma of width  $l$  and cross sectional area  $A$  then has a capacitance  $C = \epsilon_i A/l$  that is negative, corresponding to an impedance  $Z = 1/(j\omega C)$  that is inductive. In the transformed model, this element is represented as  $L_p$

Piejak, et. al have made a nice model where he has taken the above plasma considerations and proposed a circuit model which is shown on figure 3.1.1. We do not show the equations used to derive the elements of the transformer on the plasma side, although the reader is encouraged to review Piejak's paper for the details. The circuit model is particularly useful, since with the aid of a vector voltmeter or a commercially available directional coupler, one can make the necessary measurements on the primary side of the transformer and deduce many properties of the plasma.

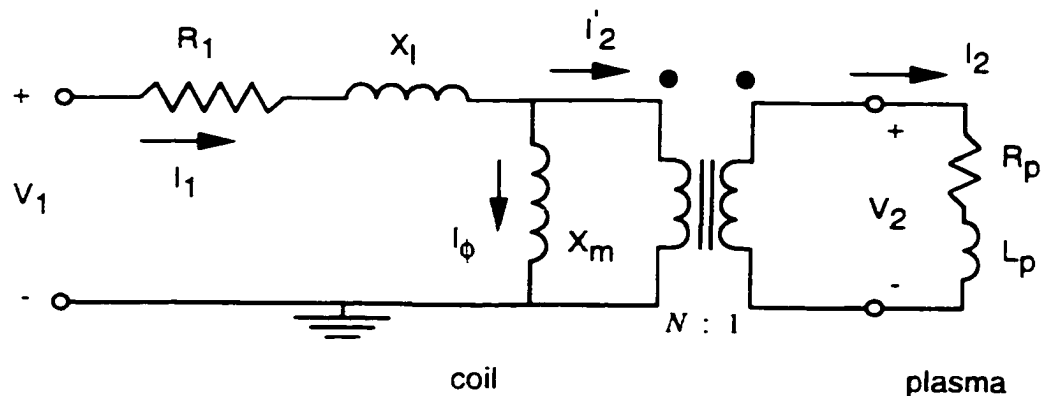


Figure 3.1.1. Circuit model for an inductive plasma from Piejak, et.al <sup>28</sup>

The transformer formalism described above shows intuitively the advantages that inductively coupled sources have in generating a dense plasma with high ionization levels. As shown above, inductively coupled rf discharges couple power through an

oscillating magnetic field. The oscillating magnetic field induces a current in a conductor such as a plasma that opposes the magnetic fields by creating an equal current flowing in the opposite direction. This is the classical transformer effect where an inductive current induces an equal current in the opposing winding. Due to the circular induced path, the loss of electrons is minimized.

Power transfer to the electrons happens within the skin depth. With inductive coupling, the electron heating occurs by the induced currents near the inductive coils where the sheath is small. Heating in the sheaths is primarily resistive in nature. Since the power to the sheath is limited approximately to the DC plasma potential drop, large amounts of power can be coupled to the plasma bulk. That is one reason why inductively coupled plasmas can dramatically increase the plasma density. The high density of the plasma in turn produces a large flux of ions that we use to bombard the target by setting up a net bias through capacitive coupling.

As previously stated, in an inductively coupled plasma, the interaction of the electromagnetic wave with the plasma occurs within a surface interaction layer. This surface interaction layer is called the *skin depth*, and it represents the penetration depth of the electromagnetic wave into the plasma. The skin depth is defined by  $\delta$  and represents the region in which the electrons are heated either through collision dissipation or stochastic processes. We note that in our case, where the pressure is near 10 mTorr, most of the electron heating occurs stochastically, since the electrons can transverse the skin depth layer in a time that is short compared to the period of the field.<sup>29</sup>

The skin depth for a 13.56 Mhz plasma is roughly proportional to  $\delta_p \approx \left(\frac{1}{n_s}\right)^{1/2}$  which for a plasma density on the

order of  $10^{11}$  /cm<sup>3</sup> is about 1 centimeter. Therefore the electrons are heated in the region near the window through which the magnetic field passes. Although the heating is confined to 1 to 2 cm, the hot electrons can diffuse to about 5 cm at 5 mTorr, so that they produce a glow over a much larger volume. At low powers, the coupling is primarily capacitive and not very efficient. As the power increases, and the plasma density increases, the inductive coupling dominates the power transfer to the plasma. There is also an upper limit for operating at very high plasma densities, where the efficiency once again falls off. The poor transfer efficiency to the plasma at very low and at very high densities is once again analogous to the well known property of an ordinary transformer with an open and shorted secondary winding.

In summary, inductive coupling is very efficient at allowing power to be coupled into a low-pressure gas. At low pressures, the plasma sheath is relatively collisionless, leading to a highly directed ion bombardment. For example, in a 5 mTorr, high-density discharge, 1-5% of the ions suffer collisions within the sheaths. The ions can still have a random energy component greater than that of the neutrals as the ions suffer collisions in the pre-sheath region, even when the sheath is collisionless. Nevertheless, we have shown why an inductive plasmas is a robust method of producing a fairly constant supply of ions which can then be accelerated to enhance the sputtering capabilities of a capacitively coupled system.

### **3.2 Plasma Characterization Techniques**

As early as 1924, the charged species in the plasma could be characterized following the pioneering work of Langmuir. In his

work, it was established that the charged species concentrations could be measured by applying a potential to a wire inserted into a plasma and measuring the current drawn from the plasma. The system by which this wire "probed" the plasma became known as a Langmuir probe.

In general, a Langmuir probe can be comprised of any symmetrical surface in contact with the plasma. The metal surface has to be connected to a variable voltage source and the area of the metal surface must be known. There are several geometries that are used, but typically they are either planar, cylindrical or spherical. In this thesis, we use the results obtained from a cylindrical probe. The most obvious reason for using this geometry is ease of construction. A simple wire and a power supply is all that is basically needed.

To use the probe to characterize the plasma, the voltage is swept from negative to positive or vice versa. Typically one sweeps from negative to positive so as to avoid the large currents that flow when the probe is positively biased. The result is a curve that represents the I-V characteristic of the plasma. A representation of a single Langmuir probe I-V characteristic is displayed in figure 3.2.1.

There are several regions on the curve that are fairly apparent. Region 1 is called the ion saturation current region as most of the plasma ions are positive and attracted to the negative potential. Region 2 is the transition region, since the ion and electron currents become balanced and the current is zero. The potential on the voltage axis corresponding to zero current is called the floating potential ( $V_f$ ). Region 3 is associated with positive probe bias so that the current is primarily electrons. Region 4 is due to the effective collection area of the probe that increases with increasing voltage. The kink in the I-V characteristics separating

regions 3 and 4 corresponds to the plasma potential, at which the probe starts becoming the "new" cathode.

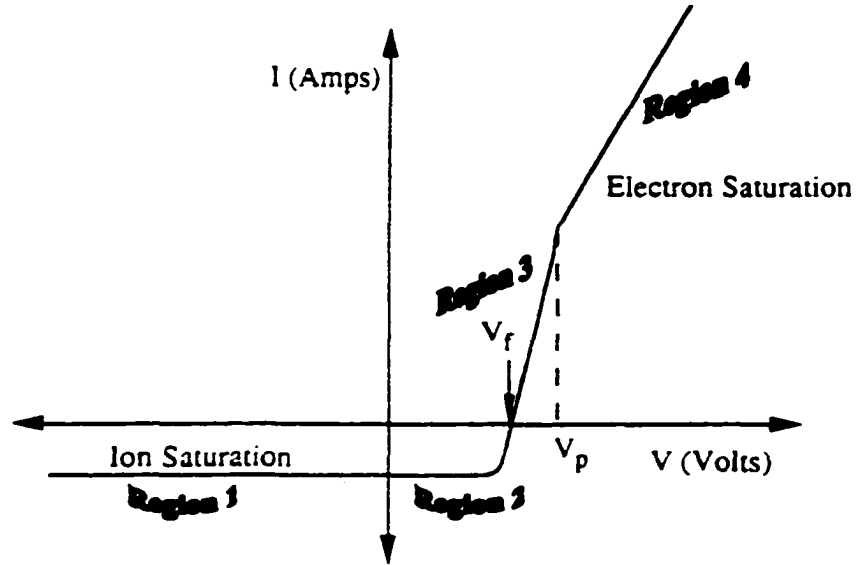


Figure 3.2.1 Typical Langmuir probe characteristics obtained with a cylindrical probe.

The main drawbacks in using a Langmuir probe is that one must know the area of collection fairly well, and that the sheath remains smaller than the collection area. For the purpose of calculating  $V_p$  and  $V_r$ , we use a cylindrical probe because the theory is better developed and a simple metallic wire is much more convenient

Since the probe is metallic, the plasma in contact with the probe has slightly different characteristics than the bulk plasma. This affects the probe collection area. Because the plasma is altered by the probe, the charged species in the bulk are also

altered. That is, if the probe is biased negatively, the field lines will terminate on the on its cylindrical surface area, skewing the results. To alleviate this problem, the knowledge of the actual probe collection area is necessary.

First, we define the sheath as the region between the probe surface and a surface in the plasma where the electric field induced by the probe is zero. Second, the Debye length  $\lambda_d$  is defined as the distance over which the plasma charges can screen charge distribution changes. If the sheath is small and all charges entering the sheath are collected by the probe, then collection area is the actual area of the probe. The sheath thickness is nearly the Debye length expressed as:

$$\lambda_d = \left( \frac{kT_e \epsilon_0}{n_e e^2} \right)^{1/2} \quad 3.2.4$$

where  $n_e = n_i$  is the plasma density. The Debye length is compared to the probe radius  $r_p$  in order to determine whether the sheath is thick

$\left( \frac{\lambda_d}{r_p} \right) \gg 1$  or thin  $\left( \frac{\lambda_d}{r_p} \right) \ll 1$ . In the thick sheath limit, the orbital

motion limited theory applies. It is important to note that in the thick sheath limit, complications arise since there will be a great deal of isotropy due to collisions in the sheath. Ions gain an energy of the order of  $T_e/2$  in the pre-sheath, which may lead to significant anisotropy. Although we assume a collisionless sheath, the pre-sheath is not necessarily so, and the pre-sheath collision with tend to isotropize the distribution of ion velocities.

In the thin sheath limit, the space charge limited theory applies. In this case, the potential drop is confined to the space charge region between the plasma and the probe. The electron velocity

distribution at the sheath edge is assumed Maxwellian and the ion temperature  $T_i$  is small compared to  $T_e$ . In contrast with the orbital motion theory, the space charge limited theory includes the assumption that all the particles entering the sheath are collected by the probe.

The saturation current collected by the cylindrical probe is found by integrating the flux to the probe tip over the distribution function at the plasma sheath edge. The interested reader is referred to Lieberman, et. al for details regarding the derivation of the solution that is:

$$I = 2en_s a d \left( \frac{2e | \Phi_F - V |}{m} \right)^{1/2} \quad 3.2.5$$

where  $I$  represents either the electron or ion saturation current. We note that  $I$  is independent of both the electron or ion temperatures. Hence a plot of  $I^2$  versus  $-V$  should be linear, with  $n_s^2$  determined by the by the slope of the line.

Langmuir probes can also be used to determine the electron energy distribution (EEDF)<sup>30</sup> This can be determined by double differentiation of the I-V characteristics. This technique is known as the Druyvestian method.<sup>31</sup> Following the description by Chen, the resulting expression for a cylindrical probe is:

$$g(E) = \frac{4V}{\pi A} \frac{d^2 I}{dV^2}$$

where  $g(E)$  is the distribution function and  $\frac{d^2 I}{dV^2}$  represents the second differentiation of the probe's I-V characteristics. The result

is typically assumed to be Maxwellian, through Druyvesteyn distributions often appear under special circumstances as in the case for  $H_2$  or  $He_2$  discharges.

Finally we point out that Langmuir probe measurements work best in DC plasmas, since any sinusoidal signal would alter the sheath characteristics. Techniques have been developed where an external circuit forces the probe to follow the variations of the plasma potential and increases the accuracy of the measurements. The increase in accuracy between the two methods is small and for all practical purposes insignificant to the study presented herein.

## CHAPTER 4 LITERATURE REVIEW

We have so far explained our motivation for pursuing this experiment, the basics of the plasma discharge from some elementary concepts and made the comparison of a plasma discharge to a simple electrical circuit. We have also explained some of the techniques, such as Langmuir probes, used to interpret the results obtained. With this understanding firmly behind, we now present a literature search on the topic. We will explain why this study is important and review previous works on which the present study is based.

### 4.1 Why RF

The magnetic data storage industry is undergoing a trend where the recording density is increasing at a compound rate of roughly 60 % a year.<sup>32</sup> This requires, among other things, thinner insulating layers, so called gap layers, between the pole pieces, and between the shields in the case of a magneto-resistive (MR) head.

The detector in an MR head is a Ni-Fe film on the order of a few hundred Angstroms, and is surrounded by other hard insulating materials such as aluminum oxide. In fact, a typical head is composed of 90% to 95% aluminum oxide, where it is used as an electrically insulating and protective material. The base coat is typically on the order of 5 $\mu$ m to 10 $\mu$ m, whereas the topcoat is typically on the order of 40 $\mu$ m to 60 $\mu$ m. Although the trend today is for thinner base and topcoats, aluminum oxide still makes up most of the thin film head.

The manufacturing of the head is typically done by RF sputtering of aluminum oxide from a solid target. This is an old technique that works well but is fairly slow, requiring up to 20 hrs

to deposit the topcoat. Moreover, to achieve these rates large power densities are required as well as complicated schemes to cool the chamber and target. Large power densities translate to large substrate biases, which can create particle problems as well. The target material is hot pressed aluminum oxide, which upon sputtering at large DC biases can create particles that get trapped in the film. And, unless oxygen is added to the sputtering atmosphere, the deposited film will be oxygen deficient with a resulting property degradation.

This leads to reactive sputtering, which seems like a simple enough process that can lead to very high sputtering rates approaching that of solid metal targets. All one has to do is to sputter a pure aluminum target in an argon atmosphere, while at the same time, oxygen is added to the sputtering. Two issues arise with this approach. First, the formation of a highly insulating coating on the target leads to charge build-up and arcing. Second, a large depression on the oxidation rate due to target oxidation. As oxygen is added, an oxide film will form on the substrate *as well as on the target*, and this is where potential problems may arise.

Recall that reactive sputtering is a DC process. Large powers are deposited into a solid metal target. In the case of Al immersed in an O<sub>2</sub> ambient, an oxide will almost immediately form on the bare target. What happens, then, is that the DC power begins to store charge on the dielectric formed on the metal target. If the potential stored on the dielectric drops below the discharge sustaining value, then the plasma is extinguished. One can temporarily alleviate this problem by increasing the DC potential, but this often leads to arcing. In summary, when oxide covers all of the target surface, the target is said to be "poisoned," and the deposition rate from the poisoned target is much slower, since the deposition rate of Al<sub>2</sub>O<sub>3</sub> vs Al is 5 to 10 times slower. The fact that such a great

difference exists on the sputtering rate between Al and AlO<sub>x</sub>, is best explained by a study partially sponsored by Advanced Energy to explore the advantages of pulsed power deposition of oxides. Figure 4.1.1 shows the dramatic change that occurs as the target changes from fully conducting to insulating.

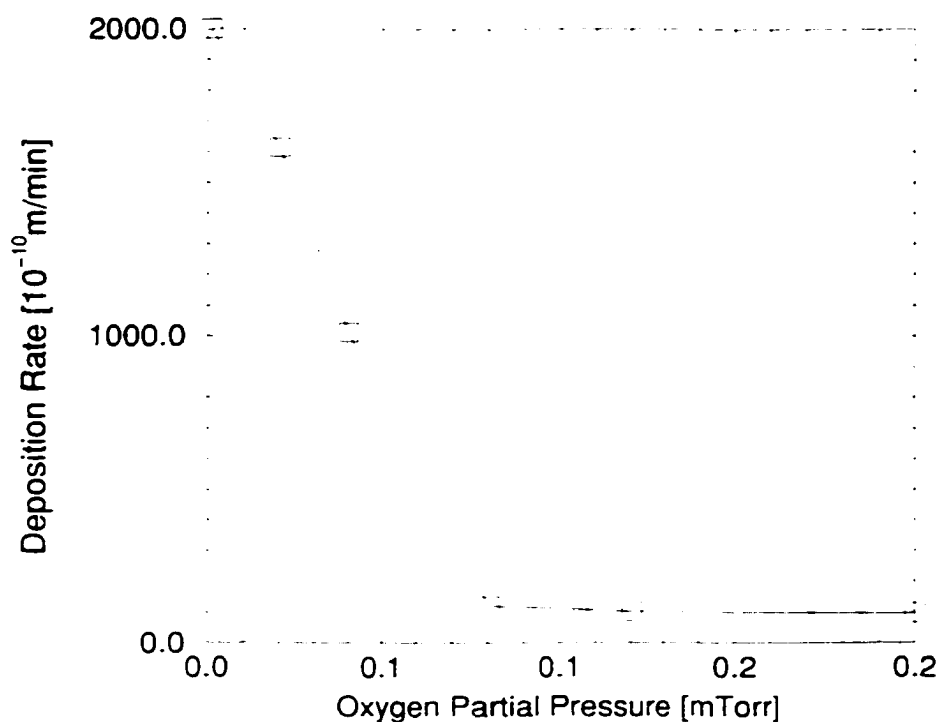


Figure 4.1.1 The deposition rate of AlO<sub>x</sub> as a function of the reactive gas partial pressure - after Sproul, *et.al.*<sup>33</sup>

When the deposition rate drops, consumption of the reactive gas is reduced, because there is less metal to react with the reactive gas, and the partial pressure of the reactive gas in the chamber increases. The amount of the increase can be quite significant. Initially, when the flow of the reactive gas is low, all the reactive gas is consumed by the reaction with the metal or is pumped away. However, when the target becomes poisoned, the

sputtering drops rapidly. Due to the lower sputtering rate, less reactive gas is consumed, and its partial pressure increase to a much higher level. A typical hysteresis loop for the reactive sputtering of metal in an Ar/O<sub>2</sub> atmosphere is shown on figure 4.1.2 below.

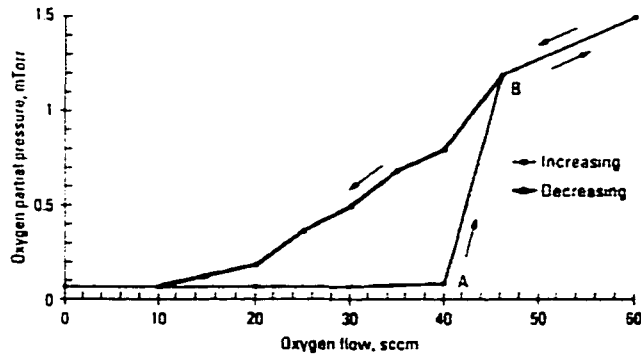


Figure 4.1.2 Typical hysteresis loop in reactive sputtering of Alumina.

The highest sputtering rates for deposition of alumina is obtained by applying a DC potential to the cathode. AC can also be used, but the average potential is roughly half that of DC. That being the case, most people choose DC to reactively sputter from a solid Al target in an O<sub>2</sub> ambient. The issue that often happens is that of arcing when the potential on the poisoned layer on the target surface is sufficiently high.

Arcing is highly undesirable as it can lead to particle ejection, which degrades the quality of the deposited film and can also damage the power supply. As already mentioned, AC power overcomes the charging and arcing problems, but RF power is not as efficient as the DC power. For an equivalent amount of power, the deposition rate from DC is approximately twice that from RF power. The main and simplest reason is that for DC power, the ions see the

full potential across the sheath while AC, there is an averaging inherent, since the potential swings between a maximum and a minimum point.

To alleviate these issues pulsed DC power has started to be used. In the past few years, it has been shown that pulsed DC power can overcome the arcing problem that were associated with reactive DC sputtering on non-conducting materials. Pulsed DC power supplies a negative pulse to sputter the target surface, but then it switches back to a positive pulse for a short time to attract electrons back to the target to discharge it. The switching back and forth between the negative and the positive polarities allows the DC power to be used very successfully for the reactive sputtering of non-conducting materials such as aluminum oxide and titanium oxide. Sproul has shown successfully that aluminum oxide coatings can be sputtered using this scheme.<sup>34</sup> All coatings were deposited on a floating substrate and all compositions of  $AlO_x$  where  $0 < x < 1.5$  were deposited. Clear film was obtained on an oxygen partial pressure of 0.08 mTorr. The film was amorphous with the clear film hardness of only 830 kfg/mm<sup>2</sup>. Additionally, the authors took exceptional steps to prevent arcing by using an automatic feedback control of reactive gas partial pressure.

Nevertheless, this pulsed power scheme is rather complicated and it still suffers from all the drawbacks associated with DC sputtering when the target is poisoned. Ideally, one would like to have the situation where the deposition rate of the oxide parallels that of the DC of solid metals but without all the complications and dangers of target poisoning.

## 4.2 Properties of Alumina

The current interest in the deposition of alumina stems from the fact that this material is quite thermally stable. Alumina is very dense and exhibits mechanical stability even at temperatures up to 1000 C°. It is also quite a hard material and most resistant to chemical attacks. Due to its density and inertness, alumina makes an ideal material for applications to the semiconductor industry as a passivation layer, especially in those areas where radiation resistance is a must. Unfortunately, it is also very difficult to deposit. Reactive DC magnetron sputtering is the preferred thin film deposition technique for most applications. It lends itself to large-scale production of thin films of metals, oxides, nitrides, etc. Many applications rely on well-defined film properties that are critically dependent on stoichiometry. Al<sub>2</sub>O<sub>3</sub> films are of particular interest since they are generally hard and stable if they are stoichiometric. However, during reactive sputter deposition of highly insulating oxides, this is difficult to accomplish. It is also difficult to maintain a high deposition rate in an arc-free environment when thick films are desired.

Most successful attempts at depositing alumina films are usually done using large amount of power at elevated temperatures. Consequently, this greatly limits its usage as a passivation layer for semiconductor applications, since temperature levels greatly exceed the melting point of Al. Commercial usage for alumina are not just limited to semiconductors. Coatings for demanding cutting applications like high-speed milling and turning of cast iron and low carbon steels and well as coatings for magnetic head applications are also in high demand. Other uses cited in literature are for corrosion resistant coatings<sup>35</sup>, optical applications<sup>36</sup> and food packaging<sup>37</sup>. In

any of these applications, it is necessary to have a robust source capable of delivering high deposition rate.

Many polymers are highly desirable materials, having properties that include high strength with low weight and often with high visual transparency. The deposition of thin films on polymers is difficult, given the inability of polymers to tolerate high temperatures. Herein, we show that by using ionized magnetron sputtering, it is possible to deposit ceramic materials at low temperatures with the advantage of having high deposition rate as well as good control on thickness and film composition. The characteristics of the coatings generated by this method are influenced by the Ar/O<sub>2</sub> ratio as well as the plasma characteristics during deposition.

Ceramic coatings deposited on polymers are suitable in packaging applications where high gas barrier properties are needed. The requirements for the coatings in such application are adhesion and dense microstructure.

Alumina is a polymorphous material. The stable form of Al<sub>2</sub>O<sub>3</sub> is  $\alpha$ -alumina, a very hard and refractory material. In its mineral form, it is known as corundum and as a gemstone it is sapphire. The blue color sometimes associated with the latter arises from a charge transfer transition from Fe<sup>2+</sup> to Ti<sup>4+</sup> ion impurities. The structure of  $\alpha$ -alumina consists of a hexagonal hard packed of O<sup>2-</sup> ions with the metal ions occupying two-thirds of the octahedral holes in an ordered array. Ruby is  $\alpha$ -alumina in which a few percent of the Al<sup>3+</sup> is replaced by Cr<sup>3+</sup>.

Other alumina phases frequently cited in the literature and observed in PVD coating are  $\gamma$ , which has a cubic primitive cell,  $\delta$  which is tetragonal, and  $\theta$  which is monoclinic. In addition Liu and Skogsmo have suggested an orthorhombic structure for  $\kappa$  alumina which

is the only other relevant and stable phase of alumina other than  $\alpha$ .<sup>38</sup> All metastable phases transform irreversibly to  $\alpha$  alumina at sufficiently high temperatures.<sup>39</sup> Because the transformation between phases causes changes in the volume of the unit cell, such changes result in catastrophic failure of the film, which is highly undesirable.

State-of-the-art industrial CVD processes for growing  $\alpha$ -alumina requires a substrate temperature of about 1000 C°. <sup>40</sup> At these high temperatures, the choice of materials is limited to substrates that can withstand the heat. No deposition technology exists at this point capable of delivering stable crystalline material for substrate temperatures less than 760 C° <sup>41</sup>. At these rather high temperatures, the choice of materials for substrates is rather limited due to the high temperature requirements. Typical cutting tools and bearing steels would change their metallurgical properties due to carbide growth and phase transformation at  $T > 500$ .<sup>42</sup>

If a technology could be developed such that it would allow for the deposition of crystalline alumina at lower temperature it would be a tremendous advantage. This would allow for the replacement of cemented carbide with steels or even plastic as appropriate substrates that could be coated with alumina. In this study, we present promising results which indicate that with some further refinements, ionized magnetron sputtering could overcome some or all of these issues. We were not able to achieve any type of crystallinity on any of the samples. However, we found a strong electron beam component that may deliver the energy necessary that would allow for deposition of polycrystalline material. Main stream deposition techniques such as CVD and sol gel technology, substrate temperatures between 1000 C and 1300 C are required to supply the

growing films with sufficient thermal energy to achieve close to thermodynamic equilibrium conditions.<sup>43</sup>

#### 4.3 Survey of Previous Studies

Considerable work has been done using RF and DC sputtering as a tool for reproducible control of film properties.<sup>44</sup> The limitation for these methods has always been the relatively low deposition rates obtainable that are normally 2 to 3 percent of the metal deposition rate for the same target. Sputtering with magnetic enhancement, however, affords the possibility of overcoming this limitation as shown by Grantham, *et. al.*<sup>45</sup> Nowicki showed a significant increase in sputtering rates from a solid target using an RF magnetron system in pure Argon using a commercial sputtering system. Rates in the order of 350 Å/min at 7.5 mTorr were achieved using the rather high power density of 7 W/cm<sup>2</sup>. Again the films were amorphous explaining why the films were rather soft.

Nowicki's study at the time it was published was important for two reasons. First, it was a systematic study on the properties of sputtered alumina with magnetic enhancement via magnetron. Second, it showed an increase in sputtering rate that could be traced to the magnetic entrapment of electrons at the target. The study also showed that addition of oxygen to the sputtering ambient helped in increasing the hardness of the film. High defect densities were found on the films grown indicating that perhaps a substrate bias could help to anneal these defects.

A year later, Gardner, *et.al* took a second look at rf sputtering of alumina from a solid target with the aim of looking specifically at the chemical and thermal-mechanical stability of such films. Additionally an RF bias was added to measure its effect on the growth kinetics. Sputtering was accomplished in pure Ar from a 99.9%

Al<sub>2</sub>O<sub>3</sub> target made by hot pressing of powder. Findings indicate that sputtered alumina in pure Ar is oxygen deficient and contains argon from the sputtering process. While RF bias may help in annealing damage, samples grown with -160 V and -120 V showed a 10% and 8% weight loss respectively when heated to temperature between 780 C<sup>o</sup> and 1000 C<sup>o</sup>. The likely cause was subsequent release of trapped Ar at these elevated temperatures that leads to degradation of the film's mechanical characteristics.

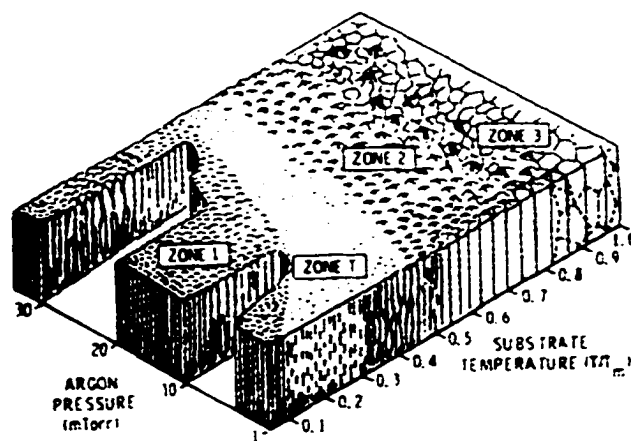


Figure 4.2.2

Thornton's structure-zone model for sputtered films.  $T$  is the substrate temperature and  $T_m$  is the coating-material melting point.

In 1995, Cuff, *et.al.* did a study on the properties of RF magnetron sputtered alumina on polyethylene terephthalate (PET) with the intention of quantifying the film characteristics for different RF powers and pressures.<sup>46</sup> PET was selected as a substrate since it is widely used on packaging applications. Ceramic coatings such as alumina deposited on PET provide the polymer with the dense microstructure necessary for high gas-barrier properties. Once again, a commercially available reactor was used and alumina was sputtered from a solid target in an Ar/O<sub>2</sub> ambient.

Predictably, the films were amorphous in the RF power range used (0.1 to 5.1 W/cm)<sup>2</sup>. Pressure had a significant effect on the density of the film. The lower the pressure, the higher the energy of the atoms sputtered from the target, which in turn inhibited the columnar structure of the film. The evolution of the structure of the alumina coatings was found to follow Thornton's structure model shown on figure 4.2.2.<sup>47</sup> Power played a similar role, leading to denser films as the higher power densities were used. Unfortunately the higher powers also lead to higher film stresses and eventually peeling. Of interest is that the researchers also reported an increase in the trapped Ar in the film as the power was increased, which was not seen in our experiment.

Two years later, Schneider successfully integrated DC magnetron sputtering with ICP confinement as tested on Rossangel and Hopwood's earlier work.<sup>48</sup> Previous studies had shown the importance of ion bombardment on the film density and ICP provided the necessary degree of plasma ionization to increase film hardness and possibly crystallinity. Alumina coatings containing the  $\kappa$ -phase were deposited at temperatures as low as 370 C. This was accomplished by setting the substrate temperature between 370 C and 430 C and reactively sputtering in an argon/oxygen ambient. The total chamber pressure was 28 mTorr. The partial pressure of oxygen in the chamber was 0.4 mTorr, which corresponded to a flow of 2 sccm. Changing the power to the ICP while maintaining all the other variables unchanged varied the total current to the substrate.

Schneider *et.al.* has shown experimental evidence whereas higher ion currents lead to phase transformations at lower substrate temperatures. Through X-ray diffraction, they were able to correlate empirically the ion current density to the target with the crystalline phase appearance. From this evidence one can extrapolate

that charged particle bombardment imparts energy that enhance crystal growth in a similar fashion that substrate heating does. Voevodin. et. al. arrived at the similar conclusion while studying the formation of crystalline TiC and TiCN at substrate temperatures of 100 C by laser ablation.<sup>49</sup> The film phase was found to be a function of both the ion flux and the ion energy. The composition of the films was found to be close to stoichiometric.

Our system was built with the aim of integrating all the knowledge mentioned above time into a robust source capable of delivering high deposition rates with the minimal hardware complexity. We built our IMS sputtering apparatus because of the general consensus that it creates a rather large and controllable source of energetic particle bombardment, and this is necessary to improve film characteristics. In principle, energetic particle fluxes can be used to form crystalline alumina at non-equilibrium conditions. However this is not a well-researched area, and there is a strong need for a systematic study as presented here.

We now know the theory and motivation behind this study. We have explained the research previously done and analyzed why our approach is different and has value. We now proceed to explain the experiments in detail and analyze the results obtained.

## CHAPTER 5 FIRST CONFIGURATION

In this chapter we present the proof of concept and the sputtering results in pure Ar. We show the deposition characteristics of alumina films sputtered from a solid target of sintered  $\text{Al}_2\text{O}_3$ . We evaluate the primary plasma factors and their interactions on the sputtering rate. We then present an analysis of variance from which we construct a model of the growth conditions.

Much of the theory and experimental history mentioned on chapter 4 is used as background to develop a source that produces thick, stoichiometric films. To accomplish this we use a combination CCP and ICP technique similar to Schneider's with the notable difference that we use rf for both the inductive and capacitive components to overcome the problems associated with reactive sputtering. The advantages of energetic particle bombardment on film properties have been empirically shown to stimulate crystal growth so that the ability to independently vary the capacitive and inductive power is essential. By setting the CCP power we set the energy of the impinging ions and by varying the ICP power, we change the substrate ion current which Schneider showed to directly affect film properties. Through careful experimentation and proper system cooling we show on this first set of experiments alumina sputtering rates around 200 Å/min at only 3 W/cm<sup>2</sup>. We compare these results with those cited in the literature and find that they compare favorably.

### 5.1 Technical Approach

The chamber design used in this experiment allows for the ability to independently set the plasma density and the sputtering potential. When we set the target power at a certain level, we have a large fraction of alumina sputtered from the magnetron. As this flux

of material passes through the inductive zone, a large fraction of the material can be ionized. By grounding or even negatively biasing the substrate, these ions arrive at the surface at a nearly normal incidence. Reports on similar set-up as ours have reported ionization rates as high as 80% of the sputtered material at a chamber pressure of 25 to 35 mTorr. Probe measurements done on our system corroborate this conclusion.

In our experimental sputtering system, we have the ability to have the substrate either floating, grounded or with a bias. Our experiments were conducted with the substrate grounded. The energy of the ions impinging the surface is nearly equal to the plasma potential minus the substrate potential. The substrate was grounded which sets the substrate potential to zero. Consequently, the energy obtained by the ionized species across the sheath is roughly that of the plasma potential minus the grounded substrate. Neutral species generated in the target sputtering process also transfer a significant amount of energy to the growing film. It is known that the kinetic energy spectrum of the sputtered neutrals has a strong peak at energies of a few eV and a long tail up to energies on several tens to hundred eV.<sup>50</sup> Studies conducted on oxide sputtering found neutrals with energies up to the full target potential.<sup>51</sup> <sup>52</sup> Supposedly, these species are generated as negative ions, are accelerated in the cathode potential and undergo a charge exchange collision en route to the substrate. The average energy of the neutral flux is a function of the amount of scattering in the gas phase and is well known to have a strong influence on the film microstructure, and hence, its properties.<sup>53</sup> The chamber pressure affects the energy of the molecules through collisions. Therefore chamber pressure is one of the factors that was initially varied and then set to the optimal level for the rest of the experiments.

The substrate temperature also has a major influence on the properties and growth structure of alumina. However, the substrate temperature has to be quite high before its effects become apparent. Consequently no attempt was made to control the temperature while the ion flux to the substrate was varied by inductive means. The starting deposition temperature for all samples was 25 C°. It was found through a thermocouple that the substrate temperature rose from 25 C° to about 80 C° indicating a strong current flow to the substrate. The samples were run for 20 mins. each to obtain a film thickness great enough to measure on the alpha step. When the reactor was run for 20 minutes the temperature never increased beyond 80 C.

The majority of this study involved the construction and debugging of the source as well as overcoming issues such as sub-optimal cooling and leaky magnetic fields. The coil itself was initially wrapped around the quartz cylinder without cooling, but later it became necessary to run water through the coil to keep the temperature below the failure point of the o-rings. Two turns around the chamber were sufficient to maintain plasma on the order of  $10^{12}$  ions/cm<sup>3</sup>. Since we were sputtering a dielectric, we could put the coil outside the chamber. However this caused a lot of problems as the RF though the coil produced enough high intensity magnetic fields to interfere with all the electronic equipment being used. For this reason, the entire source had to be RF shielded by building an isolation box that sat on top of the lower deposition chamber.

A variety of ports were built on this isolation box to accommodate cooling for the solid alumina target which sat 10 mm from the coil. A flange with a groove was designed to accept the target and silicon o-rings. During the initial phases of the experiment, it was found that a small fraction of sputtering material was coming off this flange, so the entire assembly had to be anodized. Eventually water cooling to this flange also became necessary as the o-rings

regularly leaked and deformed due to the intense temperature created during the deposition cycles.

Upon obtaining a stable system, we set a baseline by performing a full factorial screening experiment to identify important plasma parameters for sputtering. A center point of 200W ICP/CCP and 20 mTorr pressure was chosen. The extreme points for RF power were 0W and 400W respectively. We then modeled the results to explore individual parameters as well as their interactions with each other. The design and analysis was done on RS/1, which is the industry standard for statistical analysis. Through regression analysis, we modeled the growth rate using the parameters, which were deemed most significant.

We used a 40-l stainless steel chamber pumped by a 50 l/s Balzers turbo-molecular pump backed by a Leybold WAU250 roots blower and D60AC rotary vane pump. The roughing pump package was initially turned on for several minutes until the pressure reached 100 mTorr as measured by the capacitance manometer. Only then was the turbo-molecular pump turned on and the final pressure monitored by an ion gauge. The base pressure of the system was  $1 \times 10^{-5}$  Torr after 5 minutes without bake-out. Argon of 99.9% purity is introduced through a 100 sccm mass flow controller. Oxygen of 99.9% purity tees off from the main argon line and the flow is controlled by a 10-sccm mass flow controller. During deposition, a 2 Torr capacitance manometer monitors the pressure. The vacuum system did not have a load-lock, so one of the side ports was used to load the samples. A butterfly valve isolated the turbo-molecular pump, so we could keep the pumps running at all times, even when the samples were loaded into the system. The system did not have pressure control, so the pressure during film growth was set by the rate of gas flow into the chamber.

The target material is composed of 99.9% pure  $\text{Al}_2\text{O}_3$  powder prepared by hot pressing from Coors electronics. Hot pressing

is accomplished by heating the pure alumina in a graphite mold at a temperature of 1650 C to 1800 C and at least 500 psi. The resulting material is fairly pure and micro crystalline in nature. The formed product has a density of at least 3.94 g/ml and a compressive strength above 450,000 psi. The target material was a disk of 85-mm diameter. The targets were bonded with epoxy to a water-cooled magnetron with a Cu backing plate. The exact intensity of the magnetic fields produced by the magnetron was not measured, although one could visually see a well-defined toroidal glow region in the resultant plasma. This water-cooled electrode drives the target. A water cooled anodized ring is used to hold the target and electrode and serves as a flange to keep the system leak tight. The substrate holder is grounded, though it can easily be converted if a DC bias is required to control the film stress properties.

We use two 1.5 kW Advanced Energy switching power supplies for the inductive coil and target. The inductive coupled rf plasma is set up by a single turn, water-cooled Cu coil of 4" diameter. The coil is located outside a quartz cylinder, which extends 8 cm above the chamber. The power to the magnetron was through a  $\pi$ -type matching network made up of variable capacitors and inductors. The inductors were also water cooled, though probably unnecessarily so. Temperature on the match network varied less than 2 C during deposition, indicating negligible losses. An Advanced Energy impedance probe was inserted between the matching network and the magnetron. This device serves a similar purpose as a Bird wattmeter, allowing one to measure target potential, current, and plasma impedance without looking into a  $50\Omega$  load. Another similar match network was used between the power supply and the inductive coil to match the plasma impedance to the required  $50\Omega$ . A Bird wattmeter was

placed between the match network and the power supply to assure of continuous maximum power transfer

The films were grown initially on 7059 Corning quartz and then grown on microscope quartz slides. A 30-second dip on methanol was used as a pre-clean treatment to make sure that the surface was properly de-greased before the start of the experiment. Compressed air was used to dry the slides before introducing the samples into the chamber for processing. Since we samples were flat slides and the refractive index an unknown variable, ellipsometry was not used to measure the thickness of the samples during the experiment. Instead, we used a Tencor alpha step to measure the film thickness. This required that a mask be put the samples to allow for a blank region on which the stylus could glide and measure the step on the growing film. The samples were initially masked with aluminum foil and later changed to polyamide strips. The polyamide allowed for a sharper transition between the growing film and the mask layer. The aluminum foil had the undesired effect of allowing film growth under the mask.

The alpha step used was manually leveled before each measurement. The leveling procedure required that there was not a significant deviation from ideal in either the x or y direction. When the full scale was set at a 1000 A, a deviation of 10% was considered a top limit before a new calibration was deemed necessary. Most of the measurements taken indicate a growth of about 250 A/min. Over a 10 minute growth time, this implies a film thickness of 2,500 A. An upper limit of 10% signified a possible deviation of 250 A of total thickness either way.

## 5.2 Analysis of results

The deposition rates for the sputtered  $\text{Al}_2\text{O}_3$  at various power densities was determined by masking the glass slides and measuring the "step" formed between the mask and the unmasked regions with an alpha-step. The effective deposition rate was then calculated from the times that the substrates was exposed to the plasma. The slides were put as close to the center of the deposition zone as possible, but radial variation did exist. Consequently the values given are somewhat less than the actual deposition rates since the peripheral deposition zones are included as well.

Table 5.2.1 gives the actual values obtained for the first configuration of the sputtering system. We note that the reactor geometry in this case had the match network over the cathode. This made the loading of samples time consuming. Moreover such arrangement severely limited the maximum throughput and made repeatable correct placement of the substrate difficult.

All the data shown below are 100% Ar ambient. Since we did not have pressure control on this case, the flow of Ar was adjusted to maintain the chamber pressure indicated in the table.

Table 5.2.1. Results of a Response Surface Experiment with power and pressure as variables and film thickness as a response.

ICP_Power (W)	CCP_Power (W)	Pressure (mT)	Dep Rate (A/min)
300	0	20	10
0	200	10	32.3
0	300	30	50.5
400	400	10	85.6
200	300	20	87.4
0	400	10	88.5
200	200	30	89.7
0	300	20	90
0	200	30	91.6
400	300	20	107
400	200	30	109
300	300	30	114
0	300	10	115
300	200	20	123
300	300	20	123
400	0	30	138
200	200	10	141
200	400	10	150
400	200	10	151
300	300	20	159
300	300	20	171
200	400	30	179
400	400	30	179
300	400	20	188
300	300	20	238
400	400	10	248
300	300	10	325

We note that the power densities used are relatively small. For one thing the diameter of the target used is 8.5 cm. This gives an area of 56.75 cm<sup>2</sup>. At the highest input powers used, namely 400 W, the power density is just 7.05 W/cm<sup>2</sup>. We also note the pressure used in our experiment, which varied between 10mTorr and 30mTorr. This is not exceptionally low, especially when we consider that most sputtering systems work at a much lower chamber pressure to

maximize the mean free path of the molecules. Pressures of  $10^{-6}$  Torr are normally used in reactive sputtering systems.

Since the inductive coil was an integral part of the source, we note that an inductive discharge is analogous to the transformer formalism presented on chapter 4. Consequently there is a preferred region of operation in which an inductive discharge will optimally work. The poor power transfer efficiency at very low and very high densities is analogous to the well-known property of an ordinary transformer with an open and shorted secondary winding. In both cases, no power is dissipated in the load (the plasma), but in both cases, there is power dissipated in the primary winding (the coil) due to its inherent resistance. This is one reason why we set the low limit on the pressure of 10 mTorr. Had we gone lower than that, the plasma density would likely not have been high enough to sustain the discharge. Additionally, we note that at very low pressures, inductive discharges become increasingly difficult to start. The theoretical explanation is somewhat difficult, but we can get some feeling of why this happens empirically.

When RF is applied to the coil, the electric field accelerates the electrons in the gas, so they follow the changing electric field fairly well. The result is that electrons move back and forth sinusoidally. Ideally one wants high gas density to have an appropriate number of ionizing collisions to sustain the plasma. Intuition would say that the higher the pressure, the more chances there are of encountering ionizing collisions. In low-pressure discharges, the probability of having ionizing collisions is lower. Nevertheless, stochastic mechanisms take over, whereby the electrons actually gain energy through collisions on the sheath with the oscillating field. Sometimes this effect is called electron "surf riding" on the incoming potential wave. Now on inductive discharges, the electric field along the coil is distributed along its length, so

that at very low pressures, there is not enough potential across the sheath for the electrons to surf-ride on them so that the plasma becomes increasingly difficult to light at low pressures. The 10 mTorr lower limit was based on experimental observations of when the plasma needed an external stimulus to light.

Let us compare our results with some results from the literature. A similar experiment was done by Nowicki of Hewlett-Packard<sup>54</sup>, the details of which have already been discussed in chapter 4. He used a planar magnetron with 10x25 cm targets of solid alumina. Target to substrate distance was 6.9 cm. Details of Nowicki's experiment is summarized on table 5.2.2.

Table 5.2.2 Properties of Planar Magnetron-sputtered Al<sub>2</sub>O<sub>3</sub> films.  
From Nowicki.<sup>55</sup>

Sample Code	Sputtering Press (Pa)	Power Density (W/cm <sup>2</sup> )	Film Thickness ( $\mu$ m)	Dep Rate (A/min)
ER 1	0.173	7	0.2826	350
ER 2	0.4	7	0.3714	350
ER 3	1.06	7	0.2481	350
ER 5	0.1333	4	0.2269	200
ER 6	0.173	3	0.3869	150
ER 7	0.133	7	1.65	350
ER 14 a	0.173	7	5.0	175
ER 20 a	0.173	4	0.27	150
ER 33	0.133	7	6.5	350
ER 35 b	0.16	5	0.56	250
ER 53 c	0.133	7	0.138	190
ER 58 c	0.133	7	5.0	175

a Sputtered in 50% N<sub>2</sub> : Ar

b Sputtered in 1% O<sub>2</sub>: Ar

c Sputtered in 50 % O<sub>2</sub>: Ar

We note that the highest deposition rates obtained are that of 350 A/min in pure Ar. The power density used in this case was 7.0 W/cm, which is very close to the highest power densities used in this first experiment. Nowicki experimented at different pressures as

noted on the table below. Pressure is significant when the power was held at  $7.0 \text{ W/cm}^2$  (sample codes ER1 to ER 3). We note that the mean free path of a gas is proportional to the reciprocal of the gas density times the collision cross section. At 1 mTorr and room temperature, the mfp  $\lambda$  in Ar is about 8 cm and most other gases within a factor of three of this. At the equivalent of 1Pa the MFP drops below the 6.9 cm. It is likely that the molecules will scatter on its way to the substrate and re-deposit elsewhere. Target to substrate distance in the above experiment was 6.9 cm, so it feasible that the higher pressure effects would be represented on the lower deposition rate.

The data from table 5.2.1 is representative of a response surface model intended to explore which factors contribute to maximizing the sputtering rate. If the experiment is designed to be performed most efficiently, and if the factors interact with each other, then a statistical approach to planning the experiment must be employed. By using a statistical design of experiments, we use a process of planning the experiment so that the appropriate data can be analyzed by statistical methods, resulting in valid and objective conclusions. The statistical approach to experimental design is necessary to draw meaningful conclusions when the factors interact with each other as is the case here.

The first step in such a set of data is to look at the ANOVA table 5.2.3. Note that in this case we are taking into account three variables and let the film thickness be the response to the changing variables. Additionally, we also look at the interaction between these variables which is important and often overlooked. We would like to be 95% confident that the variable in question is a major contributor to the change in the response variable. Any factor or interactions less than or equal to 0.05 is significant.

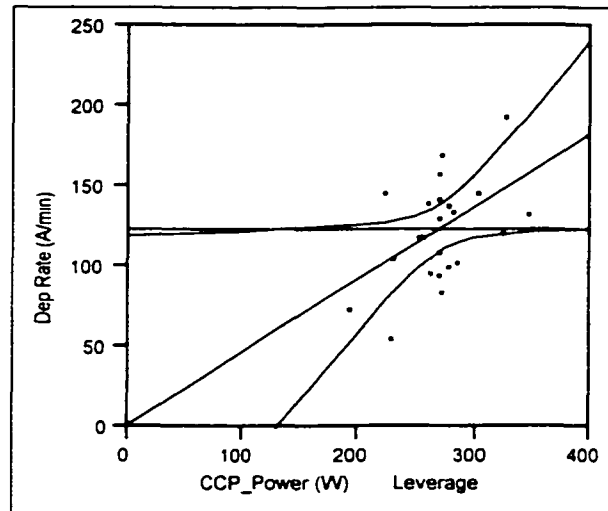
Table 5.2.3 Anova table from first set of data, 100% Ar.

Effect Test					
Source	Nparm	DF	Sum of Squares	F Ratio	Prob>F
ICP_Power (W)	1	1	1079.7555	1.0129	0.3292
CCP_Power (W)	1	1	5151.7661	4.8329	0.0430
Pressure (mT)	1	1	1785.6256	1.6751	0.2139
ICP_Power (W)*CCP_Power (W)	1	1	331.7881	0.3113	0.5846
ICP_Power (W)*Pressure (mT)	1	1	675.8760	0.6340	0.4375
CCP_Power (W)*Pressure (mT)	1	1	2090.8378	1.9614	0.1805

We note that CCP power is the most important variable, and in fact sets the sputtering rate for the system. We know this by examining the value of the F-statistic as expressed in the ANOVA table. At the 95% confidence level, any F-statistic less than 0.05 is considered significant, and CCP power comes in at 0.0430. The pressure and ICP power come next in importance. The low ICP effect on the total deposition rate is somewhat surprising. We were expecting it to play a more important role given the fact that it sets the overall ionization level. The pressure is effect is somewhat more important than the ICP to the overall response and that is expected as well. After all, one would expect that lowering the pressure would increase the mean free path of the sputtered species. We note that the distance between the target and substrate was about 3 cm in this case. We noted some deposition of alumina on the walls of the container and expected a greater contribution from lowering the chamber pressure that was apparent on the data.

Let us look at what we have just explained in a more intuitive way. Figure 5.2.1 shows the film thickness as function of CCP power. The line through the middle is a regression estimate from the data points obtained. The parabolas indicate the confidence factor of the predictor. When one goes outside the set limits, it

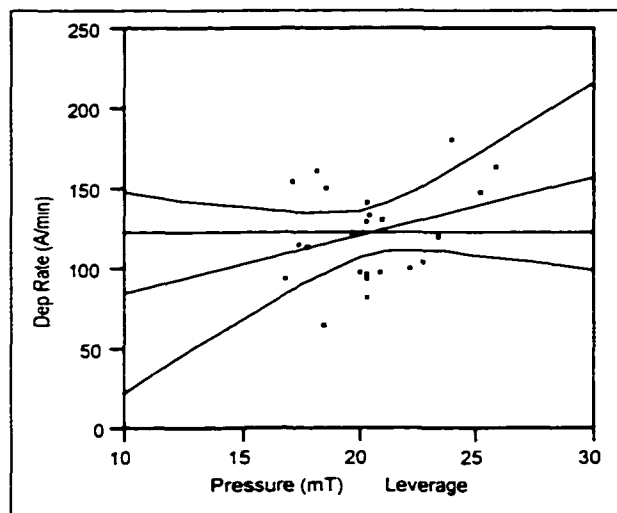
becomes more difficult to predict the results and this is evident by widening zones. Still it is easy to see how the growth rate increases as the power CCP increases.



Effect Test			
Sum of Squares	F Ratio	DF	Prob>F
5151.7661	4.8329	1	0.0430

Figure 5.2.1 Deposition Rate vs CCP Power, 100% Ar ambient

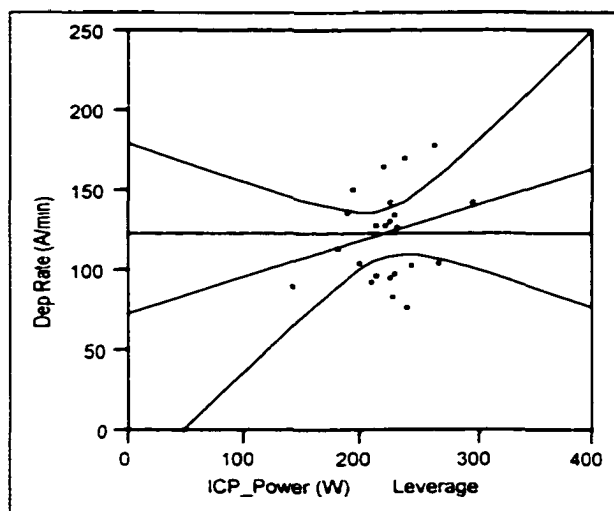
For comparison let us examine the pressure effects which Nowicki found to influence film growth. Figure 5.2.2 presents the results from our set of experiments that show some dependence as well. Immediately obvious is the fact that the best-fit regression line for the response variable is much less steep. When we vary the pressure, the response variable does not move significantly in either direction. A general trend is difficult to predict given the small variation in deposition as the pressure was lowered. In general lower pressure leads to higher deposition rates due to increased MFP, and this can be seen on the linear plots of the data 5.3.1 and 5.3.2. It is likely that the pressure changes were too small to show significance.



	Effect Test		
Sum of Squares	F Ratio	DF	Prob>F
1785.6256	1.6751	1	0.2139

Figure 5.2.2. Deposition Rate vs Chamber Pressure, 100% Ar ambient

We also show for completeness the effect of ICP power on the deposition on figure 5.2.3. The trend here is for increased deposition rate as the ICP power is increased. As mentioned above, the ICP power sets the ionization rate, so that one would expect the deposition rate to go up as the ICP power is increased.



Effect Test			
Sum of Squares	F Ratio	DF	Prob>F
1079.7555	1.0129	1	0.3292

Figure 5.2.3 Deposition Rate vs ICP power, 100% Ar ambient

We now examine the results of the regression analysis and put together a model that helps explain the effects of the primary factors on the response. The results of the sum of squares from the ANOVA are shown on table

Table 5.2.4 Summary of Parameter Estimates and Model Fit

Parameter Estimates				
Term	Estimate	Std Error	t Ratio	Prob> t
Intercept	-55.78984	69.69057	-0.80	0.4351
ICP_Power (W)	0.2278125	0.226355	1.01	0.3292
CCP_Power (W)	0.4527257	0.205936	2.20	0.0430
Pressure (mT)	3.6101276	2.789345	1.29	0.2139
ICP_Powe*CCP_Powe	0.0003319	0.000595	0.56	0.5846
ICP_Powe*Pressure	-0.004334	0.005443	-0.80	0.4375
CCP_Powe*Pressure	-0.012358	0.008824	-1.40	0.1805

Response: Dep Rate (A/min)  
Summary of Fit

RSquare	0.73358
RSquare Adj	0.633673
Root Mean Square Error	32.64938
Mean of Response	122.9565
Observations (or Sum Wgts)	23

In general, the model is a linear combination of the factors on the model multiplied by the estimators of that factor. For the above experiment, the model is expressed in the form of  $y = \alpha + \beta x + \dots$ , where  $\beta$  is one of the factors and  $x$  is the estimate of that factor. The factors are presented on column 1 and the estimator values are presented on column 2 of table 5.2.4. The R-Square value for the model is 0.73358 and it gives the proportion of the total variation of the dependent variable that is accounted for by the linear relationship with the independent variable. It can be also understood to represent the proportion of the variability in the data explained by the analysis of variance model. Thus for our experiment, the factors pressure, IC and CCP power explain about 73.36 percent of the variability of the growth rate. Since the  $R^2$  value is the ratio of the model variability divided by the total variability, we must have  $0 \leq R^2 \leq 1$ , with the larger values being more desirable.

Al<sub>2</sub>O<sub>3</sub> Dep Rate for ICP=0,200,400 W

Al<sub>2</sub>O<sub>3</sub> Dep Rate (Å/min) Contour Plot

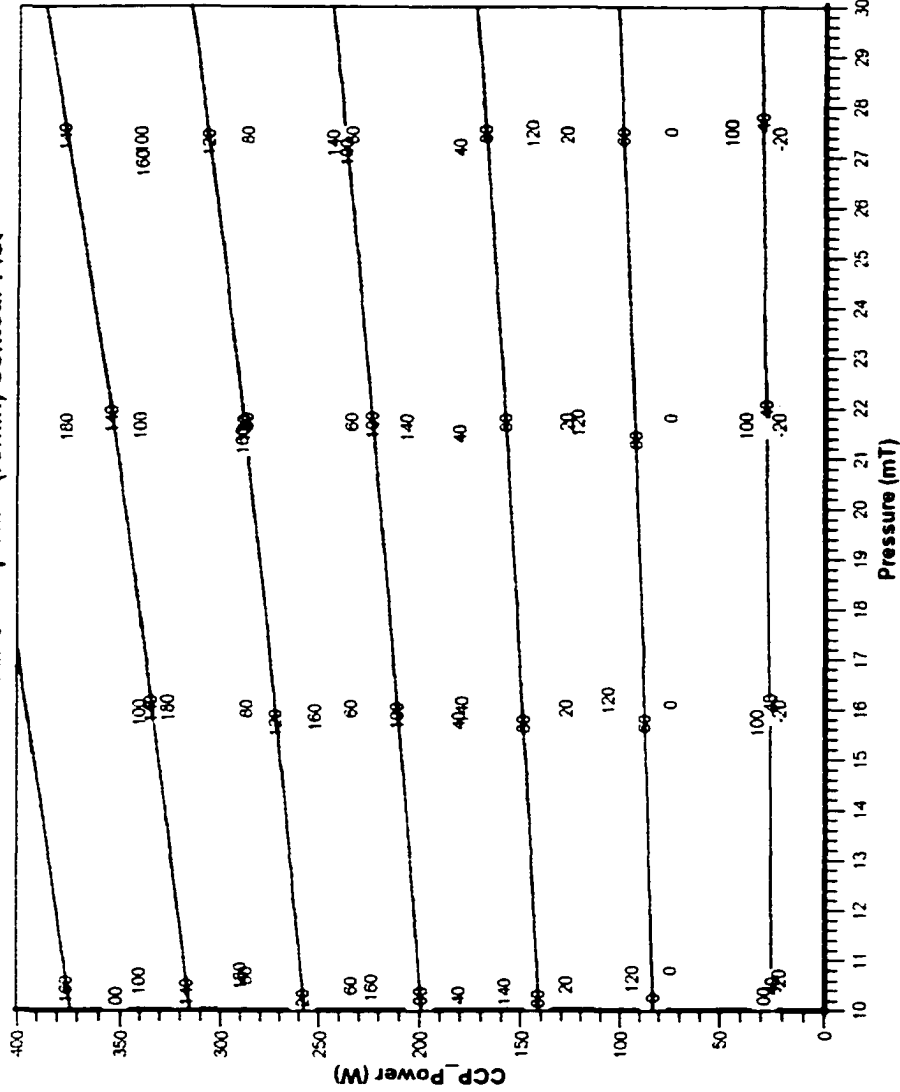


Figure 5.2.4 Contour of alumina dep rate.

Finally, figure 5.2.4 puts all the individual predictors and analysis done in a surface plot that predicts the film growth characteristics

at any level. This 2d projection of a 3d plot cleanly summarizes all the statistical analysis done in the above section.

### 5.3 An Alternative Approach

The parameters investigated are interrelated to each other in such a manner that a design of experiment (DOE) is the most correct method of drawing conclusions. However, a plot of the data in a linear fashion helps to further explain trends. For example, the chamber pressure directly affects the level of ionization. At low pressures the density is lower and the ionization decreased. One would expect the deposition be driven mostly from neutrals sputtered from the target. As the pressure is increased, the mean free path is reduced and a sputtered atom has a greater chance for re-deposition or scattering.<sup>56</sup>

The data from table 5.2.1 is re-plotted on figures 5.3.1 and 5.3.2 to gain more insight on the deposition parameters under study. The dependence on ICP power is evident as demonstrated by the ANOVA analysis shown on section 5.2. At constant magnetron power (constant alumina flux) and a constant pressure, the relative ionization climbs as a function of the RF power to the coil. The power to the CCP is clearly significant as predicted by our model. We did not see a leveling off of the sputtering rate as the CCP power was increased.

At high magnetron powers, a saturation and decline of the deposition rate has been observed by others.<sup>57</sup> This is reportedly seen at high atom fluxes through the ICP region. Such an effect was observed by Rossnagel, *et.al* during Cu deposition using a similar set-up as ours and can be explained as in the following manner. Magnetron can result is a very significant particle flux into the inductive region. For example, Rossnagel points out that the

sputtering yield for Ar on Cu is about 2.5 at 500 V. A 2 kW magnetron discharge at 500 V (4 A) yields a Cu atom flux of  $6 \times 10^{19}/s$ , which is equivalent to 140 sccm. Each of these atoms has the capability to absorb (and emit) several tens eV from the electron population through excitation and ionization. The effect of the metal flux is to depress the electron temperature even though the density may increase. Most inert gas processing-scale plasmas have a fairly low degree of ionization of the background gas, typically on the order of a percent or less. The plasmas are approximately Maxwellian, with an electron temperature in the eV range, and the rate of ionization by the tail of the distribution sustains the losses from the edges of the plasma. For an Ar plasma, the ionization potential is 15.76 eV. Atoms from the alumina material have an ionization potential that is likely much lower. When an alumina molecule passes through the dense Ar plasma, its probability of ionization is much greater than a comparable Ar. atoms. The effect, then, of significant fluxes of alumina is to depress the electron temperature even though the density may actually increase.

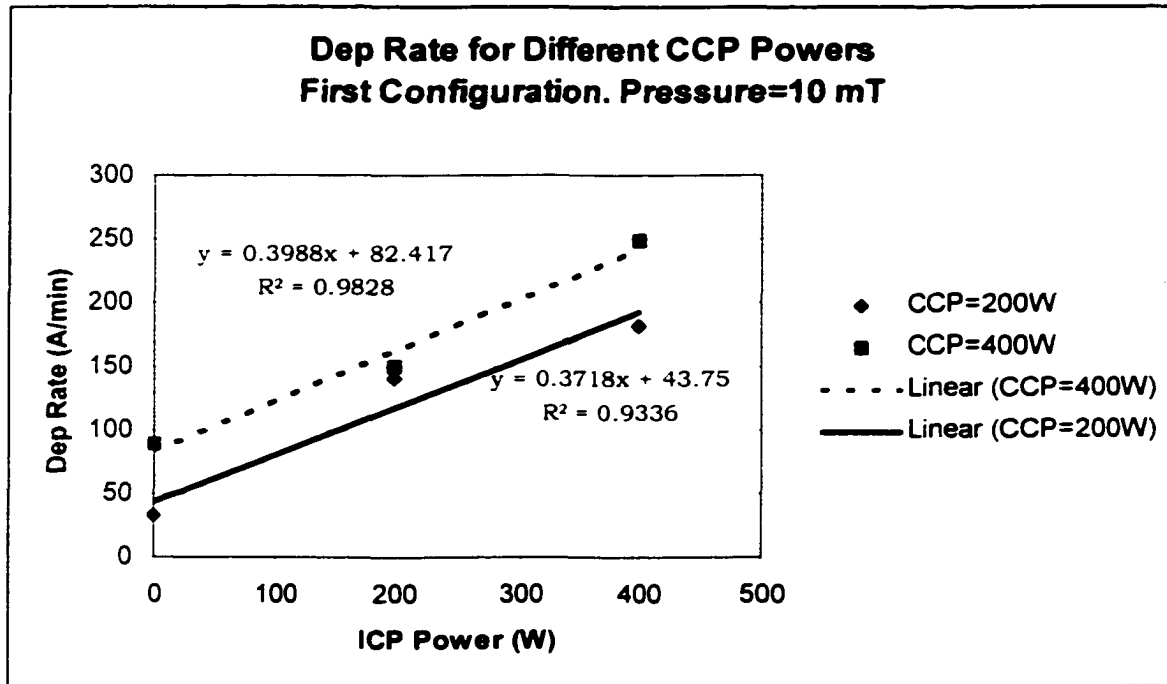


Figure 5.3.1 Deposition Rate vs. ICP power for different CCP powers, chamber pressure=10mT.

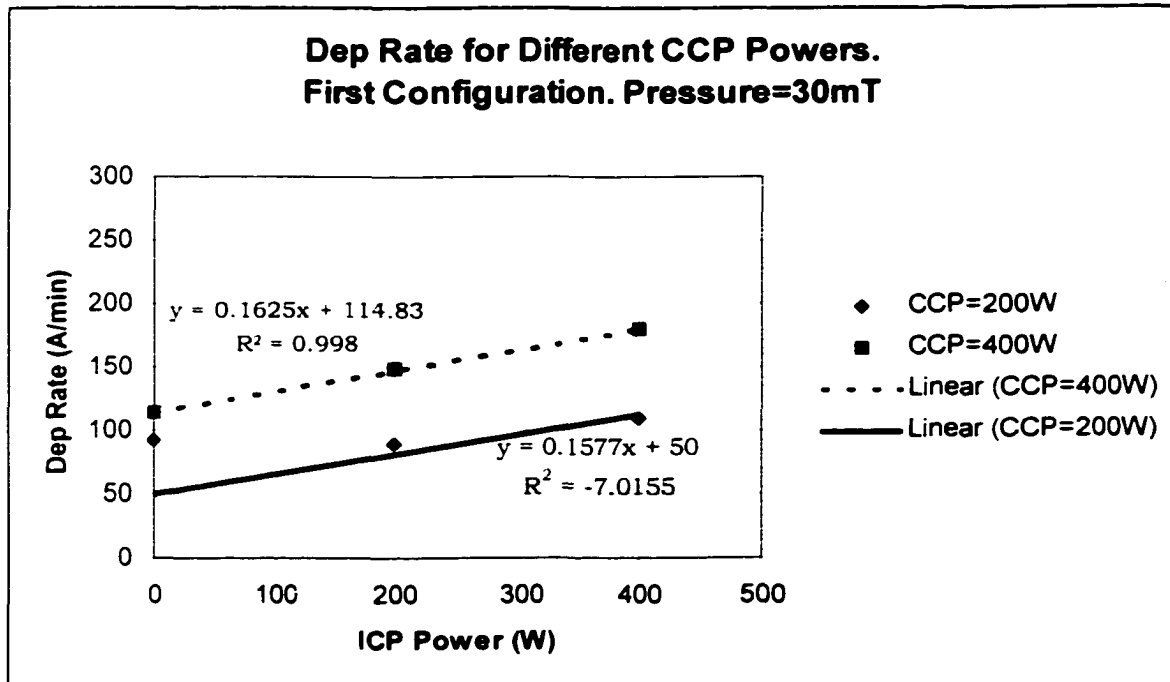


Figure 5.3.2 Deposition Rate vs. ICP power for different CCP powers, chamber pressure=30mT.

## 5.4 Conclusions

In this chapter we have presented the results obtained from a screening experiment designed to test the concept of a new sputtering source that combines magnetron sputtering with inductive coupling. The data presented herein was also presented as a poster on the 49<sup>th</sup> meeting of GEC conference in Chicago, IL. in 1997. Feedback from reviewers on the poster revealed insights on how the process could be improved

In summary, we have shown our system to be capable of independent control of plasma density and ion energy. We have shown the ability to obtain high sputtering rates comparable to previous studies. We have shown that sputtering rates increase as the CCP is increased and that ICP power increases the sputtering rate by increasing the plasma density. Finally, we have shown pressure to have a limited effect on the sputtering rate by modulating the MFP of the species.

Experimental ideas obtained at the GEC conference along with changes on the chamber designed to enable it to be run longer times were incorporated on a second set of experiments. The experiments with the improved source are shown on chapter 6. In addition, we show data on the composition of the films, the effects of O<sub>2</sub> on growth dynamics and crystallinity of the films grown at low temperatures.

## CHAPTER 6 SECOND CONFIGURATION

On chapter 5, we demonstrated the results obtained from the prototype reactor. The first set of experiments presented on the previous chapter constitutes a proof of concept that can be used as a platform on which to build upon. The principle for inductive magnetron sputtering of oxides from this new system was shown. We now implement changes that make the process more robust. These improvements allow for longer deposition times designed to look at the film dep. rates and characteristics

On the configuration previously used, the match network was connected to the alumina target directly from above. Such configuration allowed for the cathode to be as close as possible to the substrate. The closer the target is to the substrate, the higher the sputtering rate that can be expected. Hence the initial configuration, where the ICP and CCP sources were near each other, was very tight. This forced the substrate holder to be too close to the inductive region. Little is known on the interaction between inductive and capacitive plasmas near the substrate. Consequently, it was decided to move the substrate away from this region. Additionally, the inductive region of the plasma was very close to the vacuum seals. The dense plasma made cooling of the o-rings difficult and ultimately became the limiting factor as to how long the plasma could be run.

### 6.1 Changes implemented

During the initial design of the source, it became necessary to shield the coils from the rest of the system. The

magnetic fields were interacting with proper control of the magnetron and other electronic systems. The issue was greatly reduced when a shielding cage was installed around the source. The cylindrical geometry replaced the original "stove top" geometry increasing the size of the source but reducing the cross talk.

The match network to the CCP consisted of variable air capacitors that placed a limit on the power that could be delivered to the magnetron. Experimental results from chapter 5 showed the importance of the CCP power to the sputtering rate. Vacuum capacitors can handle higher voltages on the ICP and CCP match networks thereby allowing higher RF input power. The ICP network was, therefore, upgraded. The  $\pi$  network for the CCP was considerably more difficult to replace given that variable inductors are necessary to match the plasma impedance to 50  $\Omega$ . The CCP match network remained with air capacitors. This means that there is considerable risk of arcing across the fins of the air capacitor when the input power goes above 600 watts.

Other changes implemented are listed below. The ability to operate the system for periods longer than 10 min. was a major throughput limiter. This was due to the lifetime of the o-ring that was extremely short and quickly degraded with temperature. The magnetron flange was left floating to prevent unwanted sputtering from here. The first few films had a silvery complexity. Initial samples analyzed with EDX indicated an aluminum rich film, verifying our suspicion. Changes implemented are listed below:

- i. The target was permanently fixed to the magnetron.
- ii. Cooling was implemented around the flange to keep the o-rings from early failure

- iii. The quartz cylinder was cut down to 4". The substrate holder was brought down to facilitate the introduction of the samples into the chamber. Consequently The distance between the target and the substrate actually *increased*.
- iv. The ICP coils were permanently attached to the quartz cylinder to fix their position.
- v. Water cooling to the ICP coils itself was implemented. This was the one significant change that allowed us to run the reactor longer than before.
- vi. An automatic controller for the CCP match network was installed. This allowed for the proper adjustment of the ICP source without having to worry if the CCP match drifted during deposition.
- vii. O<sub>2</sub> delivery capability was added.
- viii. Substrate bias capability was added.
- ix. A thermocouple was added to keep track of the substrate temperature before and after the deposition
- x. The pump package was changed to conform to the usage of O<sub>2</sub>
- xi. The flange holding the quartz cylinder to the magnetron was anodized.
- xii. An isolation valve was installed to allow the pumps (specifically the turbo-molecular) to keep on running when the chamber was brought to atmospheric conditions.

## **6.2 Analysis of results**

The methodology and details of the experiment have already been explained in detail in section 5.1. Changes implemented to the source are mentioned on section 6.1. This allowed for a more robust process capable of longer operation.

The lack of a load-lock made the repeatable positioning of the samples difficult. Additionally the pumps had to be continually turned on and off during sample loading. To address these issues an isolation valve to the turbo-molecular pump was installed and a butterfly valve to the mechanical pump was added. A vent valve was also added to help bring the system up to atmospheric pressure

The placement of the substrate holder below the coils increased the distance between the target and the substrate holder was increased from 3 cm to 12 cm, a four-fold increase. This was the minimum distance that would allow us to consistently load the masked slides on the same position without having to disassemble parts of the reactor. Increasing the substrate to target distance leads to lowered sputtering rates. Nevertheless, the change resulted only on a marginal decrease on the sputtering rate as evidenced on the experimental data.

Based on previous studies on reactive sputtering, we decided to experiment with different oxygen partial pressures to see how the sputtering rates would be affected. In reactive sputtering, it is necessary to maintain a level oxygen to react with the metal and to maintain stoichiometry. The pressure was known to have a small effect on the range of study, so we set it at 15 mTorr for all the runs. The length of a deposition run was set at 20 mins. Upon introduction of the sample into the chamber, the gases were turned on and allowed to stabilize for 5 min. The power for the magnetron was turned on first and slowly ramped to set point as well. The inductive power was then slowly turned to the set point and the match network adjusted for maximum power transfer. The deposition time started when the power to the CCP was applied.

The results from a set of runs at 15-mTorr chamber pressure in 100% Ar ambient are shown on table 6.2.1. The sputtering rate is very small when the CCP is set to zero but still present.

With only the ICP power, a sheath still exists, though the potential across it is very small. That is why one still sees some level of deposition with zero input power to the cathode.

In general the trend is for increased deposition as the CCP power is increased in accordance to previous observations. The ICP power plays a small role on sputtering rate at a low power and increases in importance at high CCP powers when the ambient is pure Ar. At high ICP power, the ionization is high, and high cathode potentials are very effective in pulling these ions towards the target for material removal

The sputtering rates are highest when the ambient is 100% Ar. A noticeable downwards trend is apparent from figures 6.2.2 and 6.2.3 as the  $O_2$  is increased, falling to nearly half the peak value when the  $O_2$  partial pressure reaches 4%. This is likely a result of adding negative ion species caused by the dissociative attachment of oxygen via  $e + O_2 \rightarrow O^- + O$ . With the presence of negative ions in the plasma we create a situation where the negative ions are trapped within the discharge by the positive potential of the plasma with respect to the all the wall surfaces. The negative ions are lost only by recombination with positive ions in the volume. This situation causes that the positive ion losses to the walls to be much lower in an electronegative plasma. Lieberman offers a detailed analysis of electronegative plasmas, but in short, the electron temperature  $T_e$  is not longer just a function of  $n_e d_{eff}$ , but now depends separately on  $n_e$  and the geometry, as well as the discharge power  $P_{abs}$ . One result is that the negative ions suppress the Bohm velocity at the sheath edge, thereby reducing is their energy.

The primary factor which gives a feeling of the electronegative interaction is  $\alpha$  or the ratio of negative ions to the total electron density. Since our system is working a low

pressure and the oxygen flow is relatively low, we could argue that the negative ion density is small and concentrated within the plasma volume. We can then assume that the plasma edges behave essentially electro-positively so that the effects are minimized. Nevertheless, the reality is that the CCP and ICP combination complicates the matter since the ICP could lead to significant levels of negative oxygen ions causing the plasma to behave erratically. This was the case as the oxygen content was increased. The plasma became increasingly difficult to match for maximum power transfer. At the highest oxygen flow, we could not completely match the plasma impedance leading to decreased power delivery on both, the CCP and, therefore, lower deposition rates.

Schneider and Sproul have observed similar results. Admittedly, these results arise from reactive sputtering, where precise control of oxygen is a necessity. Our system is completely different. Nevertheless, they do observe a hysteresis curve on the oxygen dependence so that an O<sub>2</sub> pressure increase of 5% (from 2% to 7%) decreased the deposition rate from 76% to 38% of the metal deposition rate.<sup>56</sup> In our case, there may also be a peak O<sub>2</sub> content between zero and two percent that was missed in the experimental design. Nevertheless, the results presented herein agree with those observed elsewhere.

Figure 6.2.1 show the sputtering rate as a function of target power for different ionization levels. The trends show how denser plasmas contribute to increased Al<sub>2</sub>O<sub>3</sub> deposition rates. The correlation is excellent as indicated by the R<sup>2</sup> regression statistic. When O<sub>2</sub> is added to the gas mixture, the CCP trend remains, but the ICP contributions declines due to the plasma instabilities already mentioned.

Table 6.2.1. Sputtering rate (A/Min) in 100% Ar ambient, chamber pressure at 15 mTorr

ccp	icp=0	icp=100	icp=200	icp=300
0	0	10	10	15
400	30	46.25	50	75
500	45	60	81.25	70
600	50	120		190

**Sputtering rate as a function of target potential.  
100 % Ar ambient**

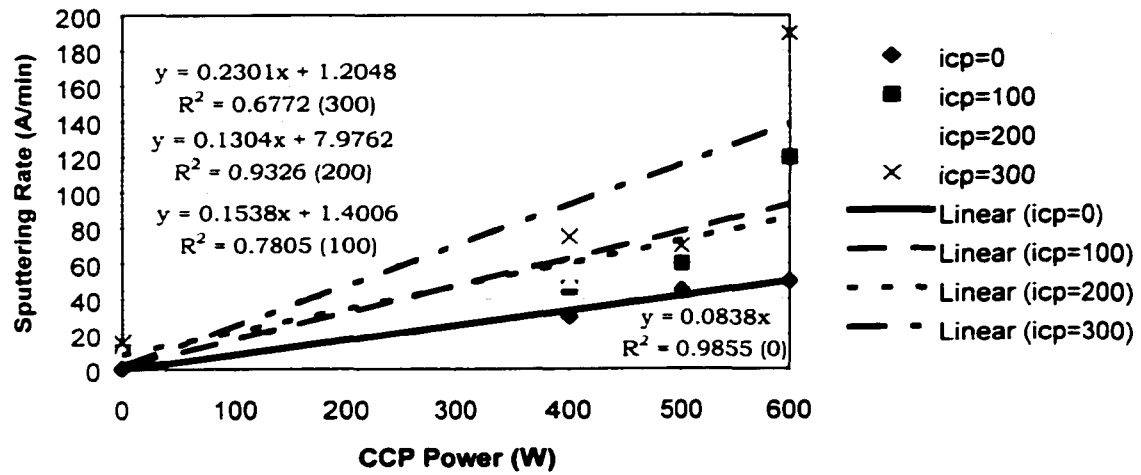


Figure 6.2.1. Alumina Sputtering Rate (A/min) in 100% Ar. Chamber pressure 15 mTorr

Table 6.2.2. Sputtering rate (A/Min) in 98% Ar ambient and 2% O<sub>2</sub>,  
chamber pressure at 15 mTorr

ccp	icp=0	icp=100	icp=200	icp=300
0	0	10	10	15
400	50	48.75	51	42.5
500		71.25		47.5
600	110	95	87.5	77.5

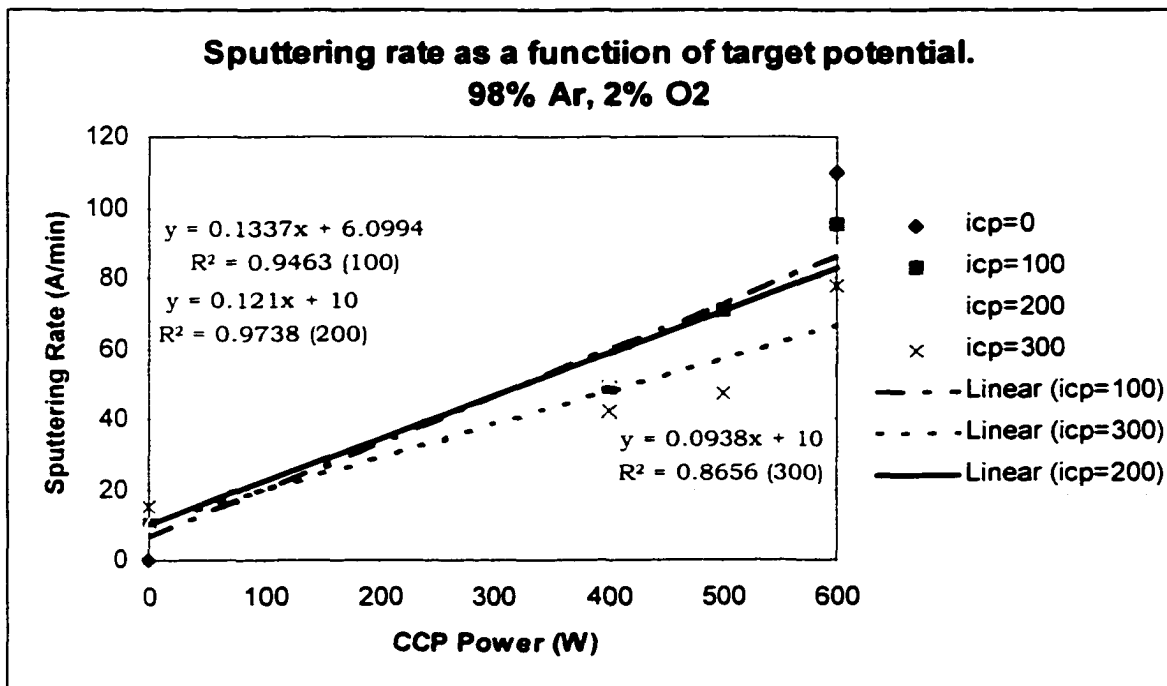


Figure 6.2.2. Alumina Sputtering Rate (A/min) in 98% Ar and 2% O<sub>2</sub>,  
chamber pressure 15 mTorr

Table 6.2.3. Sputtering rate (A/Min) in 96% Ar ambient and 4% O<sub>2</sub>, chamber pressure at 15 mTorr

ccp	icp=0	icp=100	icp=200	icp=300
0	10	10	12.5	15
400	40	35	25	40
500	55	46.25	47.5	42.5
600	65		65	78.75

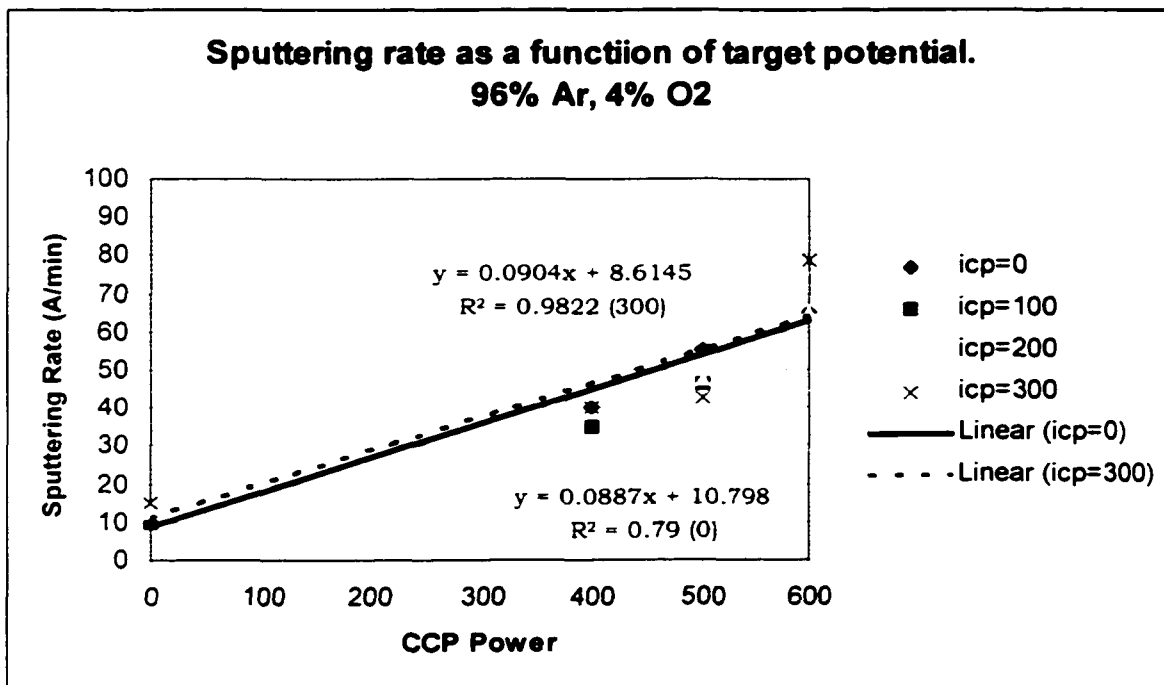


Figure 6.2.3. Alumina Sputtering Rate (A/min) in 98% Ar and 2% O<sub>2</sub>, chamber pressure 15 mTorr

### 6.3 Composition Analysis of the alumina films

Several samples were submitted for analysis to the reliability laboratory at Hewlett-Packard to judge the quality of the films and to verify that indeed the thin film grown was  $\text{Al}_2\text{O}_3$ . Four of these films were run at extreme points and are represented on table 6.3.1. The rest of the samples were run at typical set points and are detailed on table 6.3.2

For the chemical and stoichiometric analysis ESCA was chosen because it can produce quantitative results with the use of standards. ESCA (electron spectroscopy for chemical analysis) is synonymous with XPS (x-ray photoelectron spectroscopy.) It is a non-destructive technique that involves x-rays striking a sample and emitting electrons via the photoelectric effect.<sup>59</sup> Others have used RBS to analyze the film's stoichiometry since it can also provide some level of information on crystal quality. Nevertheless, XPS is well suited for the type of chemical information sought on this experiment.

ESCA is a surface sensitive technique. The fundamental parameter describing the surface sensitivity is the mean escape depth (MED), ranging between 1nm and 4 nm for most experimental situations: ~63% of the information comes from within 1x MED of the surface, ~95% of the information comes from 3x MED of the surface.<sup>60</sup>

HP's Quantum 2000 ESCA system has a circular x-ray spot with a tunable full width at half maximum between 7 and 140 microns.<sup>61</sup> It uses a secondary x-ray image (SXI, analog to a SEM image) to locate the features on the samples.

The photo-emitted electrons carry information about the composition, chemistry and work function of the sample's surface. The

sensitivity has a practical limit of about 0.1%. Oxides, nitrides silicides, halides, and others easily distinguished from the metals.

The table below lists the compositions of the films after sputtering for about 40 A. All the films had some residual C, but it was so small as to be negligible. All the films had some Ar that could have been either in the film or embedded in the film during sputtering. There is no way of distinguishing the source of Ar, but it was most likely embedded in the film during its growth. The sample used as the Al<sub>2</sub>O<sub>3</sub> standard was not particularly pure. It had some residual SiO<sub>2</sub> at very low levels.

Table 6.3.1 Percent composition obtained from ESCA on four films and a Al<sub>2</sub>O<sub>3</sub> standard

Element	Film1	Film3	Film6	Film16	Al <sub>2</sub> O <sub>3</sub>
O	67.5	69.0	65.0	66.0	68.4
Al	32.5	31.0	35.0	34.0	31.7

- I. Film1 - ICP=300, CCP=0, P=20mT, 100% Ar
- II. Film3 - ICP=0, CCP=300, P=30mT, 100% Ar
- III. Film6 - ICP=0, CCP=400, P=10mT, 100% Ar
- IV. Film16 - ICP=400, CCP=0, P=30mT, 100% Ar

In addition several other samples taken at different combinations of pressure and ICP/CCP to investigate the effects of combining both sources of power. For the samples indicated below, the ambient was 100% Ar. The samples are coded as thus:

- I. Sample #9 - ICP=200 W, CCP=200 W, 30mTorr
- II. Sample #17 - ICP=200 W, CCP=200 W, 20mTorr
- III. Sample #13 - ICP=400 W, CCP=400 W, 30mTorr
- IV. Sample #11 - ICP=400 W, CCP=300 W, 10mTorr

- V. Sample #15 - ICP=300 W, CCP=300 W, 20mTorr  
 VI. Sample #5 - ICP=300 W, CCP=300 W, 20mTorr

Table 6.3.2. ESCA composition in at. % after sputtering for 8 nm.

19732, #9	0.3	0.0	67.0	32.7	0.0
19732, #5	0.0	0.0	66.9	33.1	0.0
19732, #17	2.5	1.2	62.6	33.7	0.0
19732, #13	0.4	0.0	65.7	33.9	0.0
19732, #11	0.8	0.0	66.0	33.2	0.0
19732, #15	0.0	0.0	66.6	33.4	0.0
average	0.7	0.2	65.8	33.3	0.0
deviation	1.0	0.5	1.6	0.4	0.0

A perfect alumina film would have an oxygen to aluminum ratio of 60/40. Clearly this is not what is shown on table 6.3.2. We point out that the alumina standard of table 6.3.1 does not approach the ideal ratio either. The reason is that alumina is naturally bound to water. This is the case for all of the major phases of alumina known such as: gibbsite ( $\alpha$  -  $\text{Al}_2\text{O}_3 \cdot 3\text{H}_2\text{O}$ ), bayerite ( $\beta$  -  $\text{Al}_2\text{O}_3 \cdot 3\text{H}_2\text{O}$ ), boehmite ( $\alpha$  -  $\text{Al}_2\text{O}_3 \cdot \text{H}_2\text{O}$ ) and diasporite ( $\beta$  -  $\text{Al}_2\text{O}_3 \cdot \text{H}_2\text{O}$ ). Gibbsite is the predominant American bauxite and bayerite is artificially produced by slow carbonation by sodium aluminate. Boehmite is the naturally occurring European bauxite and diasporite is naturally occurring in Russian deposits and areas of Missouri and Pennsylvania.

In our results, we see an oxygen to aluminum ratio closer to 66/33. Assuming an atomic weight for oxygen of 16 amu and aluminum of 27 amu, the stoichiometry of the material is quite close to  $\text{Al}_2\text{O}_3 \cdot 4\text{H}_2\text{O}$ , indicating a 31% Al and 64%  $\text{O}_2$ . Ideal boehmite would have 3 $\text{H}_2\text{O}$  molecules indicating 35% Al and 62%  $\text{O}_2$ . Therefore the samples obtained are slightly more hydrated than ideal. We note that

XPS is unable to pick up H or He. Consequently, these elements, if present, would not appear on the element tables 6.3.1 or 6.3.2.

The formation of coatings with entrapped gas atoms is a common occurrence in sputtered coatings deposited at low pressures.<sup>62</sup> For example, when argon ions are incident on the target, there is a significant probability that they will be neutralized and reflected. When depositing at low pressures, the reflected and neutralized ions will reach the substrate with high kinetic energy owing to the high mean free path.<sup>66</sup> Consequently, the reflected argon atoms can be entrapped in the growing film. Nevertheless, there is no sign of Ar entrapment in any of the films examined by XPS. Possibly, the atoms lose the majority of the energy as they cross the dense plasma region between the coils.

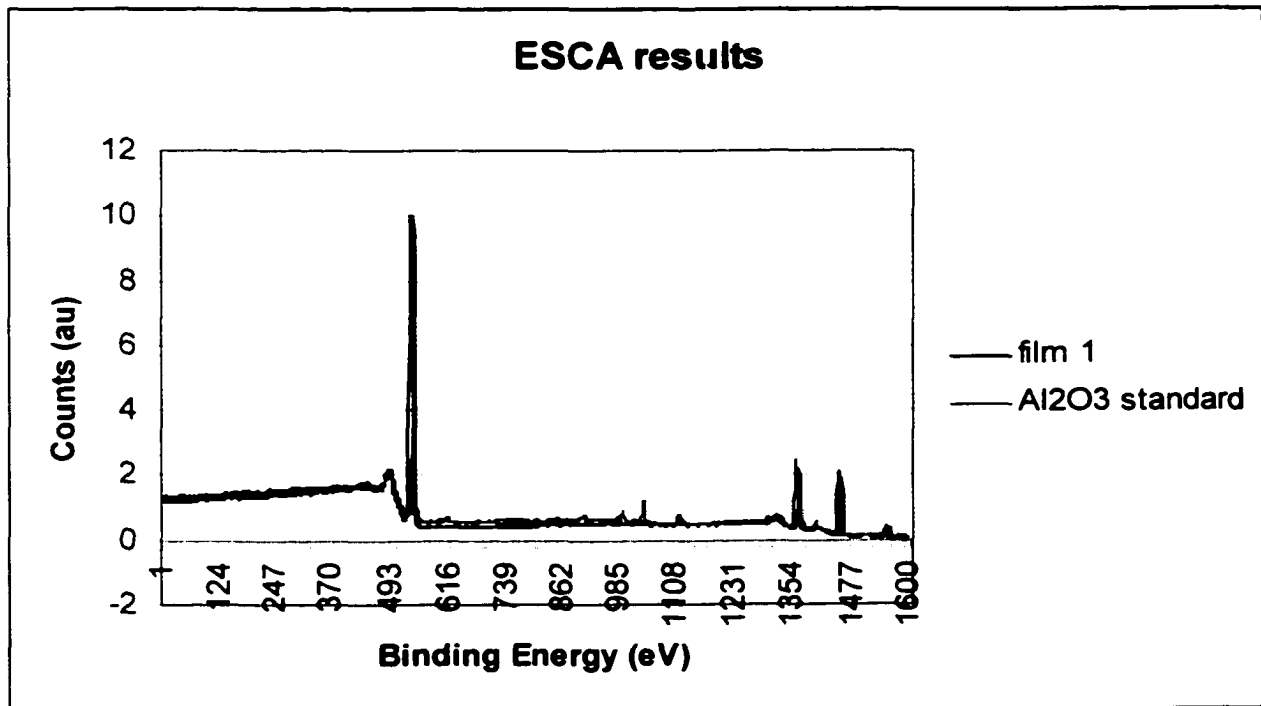


Figure 6.3.1 Film 1 compared to Al<sub>2</sub>O<sub>3</sub> solid standard. Dep parameters are ICP=300, CCP=0, P=20mT, 100% Ar ambient.

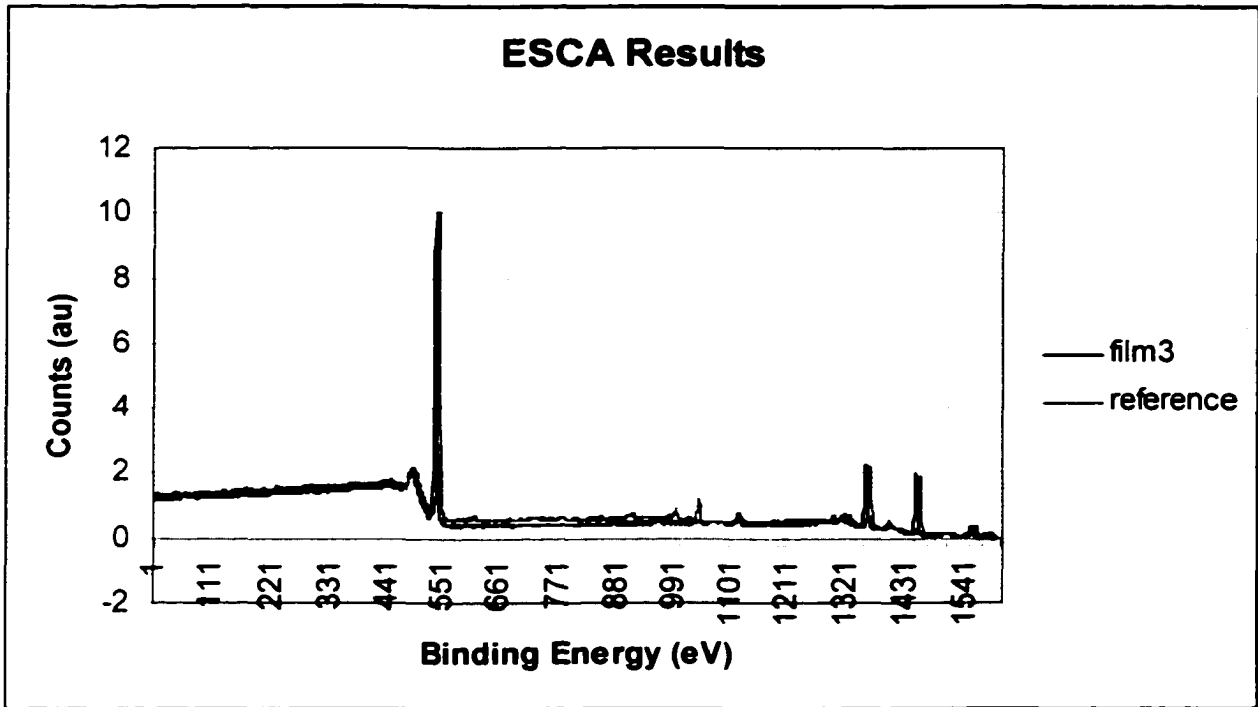


Figure 6.3.2 Film 3 vs Al<sub>2</sub>O<sub>3</sub> solid standard. Dep parameters are ICP=0, CCP=300, P=30mT, 100% Ar ambient.

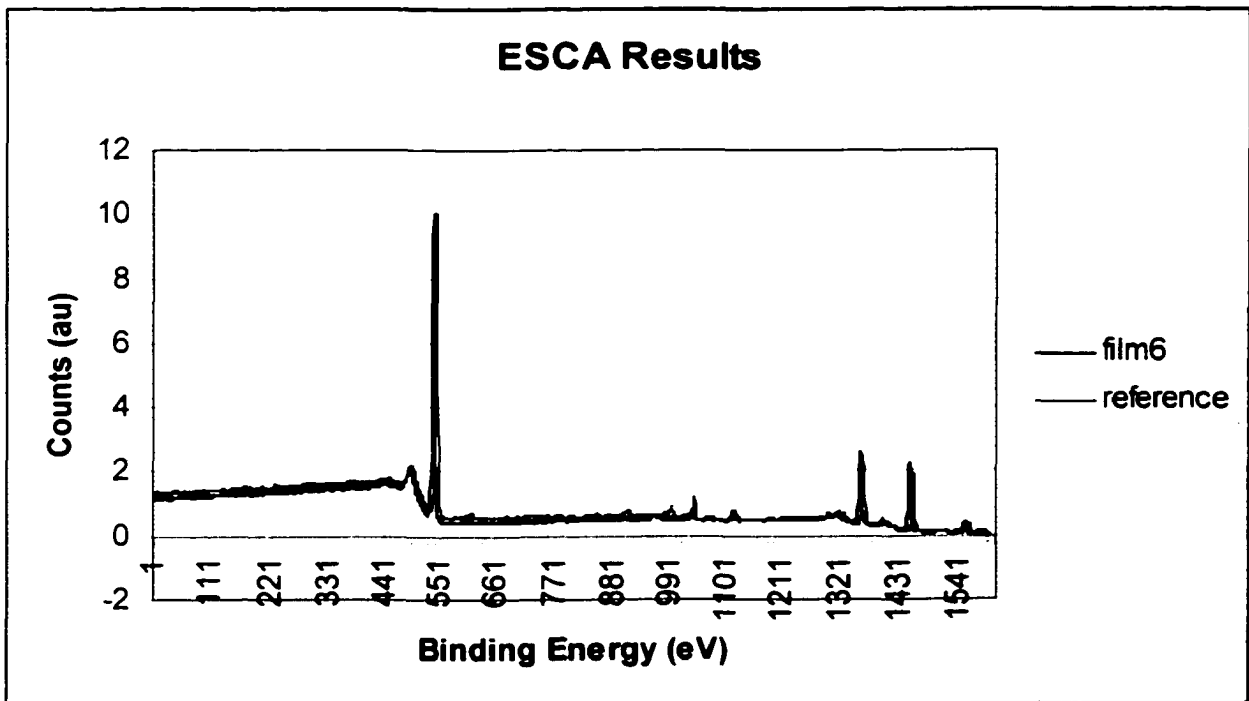


Figure 6.3.3 Film 6 vs Al<sub>2</sub>O<sub>3</sub> solid standard. Dep parameters are ICP=0, CCP=400, P=10mT, 100% Ar ambient.

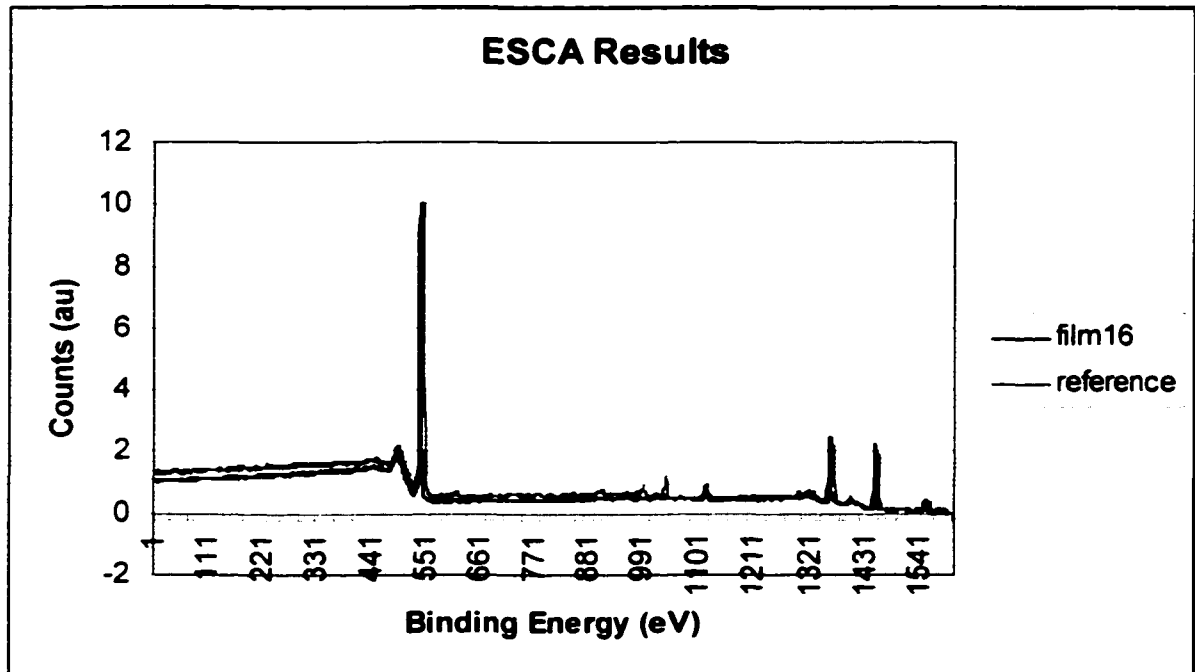


Figure 6.3.4 Film 16 vs  $\text{Al}_2\text{O}_3$  solid standard. Dep parameters are ICP=400, CCP=0, P=30mT, 100% Ar ambient.

The above figures show plots of the binding energy vs intensity for the samples indicated by table 6.3.1. Each one of the samples is then compared with the known alumina standard. In every case, the XPS analysis showed no significant difference in the binding energies of the thin films produced and the bulk alumina standard (see figures 6.3.1, 6.3.2, 6.3.3 and 6.3.4). Furthermore, no indication of free metals could be observed. Free metals will affect both the optical and mechanical properties in an undesirable way. The chemical analysis proved to be close to stoichiometric, and within the error of the measurement. No difference in composition could be detected for the different conditions at which the samples were grown.

#### 6.4 Microstructure Analysis of the alumina films

The data shown in this chapter and in the previous one indicates that this novel is source capable of sputtering at high rates and producing alumina very close to ideal. We now take a closer look at the microstructure of these films. For that we use x-ray diffraction (XRD), since it is the most widely used technique for general crystalline material characterization.

XRD is a powerful technique used to uniquely identify the crystalline phases present in the materials and to measure the structural properties (strain state, grain size, epitaxy, phase composition, preferred orientation, and defect structure) of these phases. Owing to the huge data bank available covering practically every phase of every known material, it is routinely possible to identify the phases in polycrystalline bulk material and to determine their relative amounts from diffraction peak intensities. Phase identification for polycrystalline thin films is possible down to thickness of 100 Å.

In X-ray diffraction (XRD) a collimated beam of X-rays, with wavelength  $\lambda \sim 0.5$  to 2 Å, is incident on the specimen and diffracted by the crystalline phases in the specimen according to Bragg's law ( $\lambda = 2d\sin\theta$ , where  $d$  is the spacing between the atomic planes in the crystalline phase). The intensity of the diffracted X-rays is measured as a function of the diffraction angle  $2\theta$  and the specimen's orientation. This diffraction pattern is used to identify the specimen's crystalline phases and to measure its structural properties.

The crystalline analysis was carried out using a Siemens XRD machine using a thin film diffractometer with a Cu  $K\alpha$  radiation in the Bragg-Bentano geometry. The x-ray generator settings were 40

kV and 30 mA. The step size was  $0.05^\circ$ , and the scans were acquired from  $20^\circ$  to  $60^\circ 2\theta$ .

The major difference between ionized and conventional magnetron sputtering is that the ion flux to the substrate consists of Al, Ar and O species as opposed to mainly Ar in conventional magnetron sputtering (if Ar is used as the sputtering gas). Qualitative evidence for the increasing degree of ionization with increasing power supplied to the RF coil has been shown by Schneider and independently confirmed elsewhere.<sup>67 68</sup> Consequently, the ion density at the substrate increases as the RF coil power is increased. In theory this should increase the surface mobility at the film thereby facilitating crystalline growth. Nevertheless, all the samples tested are amorphous. This is not unexpected, given that below 300 C substrate temperature, alumina coatings are reported to be X-ray amorphous.<sup>69 70</sup>

The results given here are representative of different growth conditions. For reference, we point out that there are many different phases of alumina of which corundum is the crystalline form found in nature. The stable form of  $Al_2O_3$  is  $\alpha$ -alumina, also known as sapphire. It may also appear as  $\kappa$  in orthorhombic configuration or  $\theta$  as monoclinic. The latter two configurations are less densely packed and therefore are easier to obtain.  $\kappa$  alumina is particularly interesting given that it has been deposited at temperatures as low as 380 C and reportedly has very similar plastic and elastic behavior as the more stable  $\alpha$  polymorph.<sup>71</sup> XRD data for  $\kappa$  alumina is widely available from the JCPDS data and all the other possible crystal configurations as well. A typical diffraction pattern is shown on the table 6.4.1. It is for  $\theta$  alumina, which is quite similar to  $\kappa$ .

Table 6.4.1 Aluminum Oxide, Monoclinic Standard ( $\theta$ ),  $\lambda=1.54056^{72}$ 

dspace	$2\theta$	Intensity	h	k	l
5.7	15.53347	2	2	0	0
5.45	16.25072	10	0	0	1
4.54	19.53722	18	-2	0	1
2.837	31.50938	80	-4	0	1
2.73	32.77847	65	0	0	2
2.566	34.93861	14	-1	1	1
2.444	36.74337	60	1	1	1
2.315	38.8707	45	4	0	1
2.257	39.91143	35	2	0	2
2.019	44.85642	45	-1	1	2
1.9544	46.42424	8	-6	0	1
1.9094	47.58495	30	6	0	0
1.7998	50.68039	14	5	1	0
1.7765	51.39317	6	-6	0	2
1.7376	52.63086	4	-4	0	3
1.6807	54.55763	2	6	0	1
1.6216	56.72191	6	2	0	3
1.5715	58.70333	2	-1	1	3
1.5426	59.91424	25	-3	1	3
1.512	61.25542	6	-6	0	3
1.4883	62.33884	25	1	1	3
1.4526	64.05017	25	0	2	0
1.4264	65.37148	10	7	1	0
1.3883	67.40094	100	4	0	3

The results of the phase analysis for a sample of all the films grown are shown on figures 6.4.1 to 6.4.5. The films do not show any significant peaks indicating that there is no crystalline structure to the films. For comparison, we did XRD on a flat piece of Corning quartz glass as shown on figure 6.4.6. Clearly, there is no difference between the plain slide and the ones containing the sputtered films. Crystalline samples from other studies indicate strong peaks on  $\kappa(022)$ ,  $\theta(203)$ ,  $\theta(601)$  and  $\kappa(030)$ , none of which appear in any of the samples with any intensity.

### XRD Results

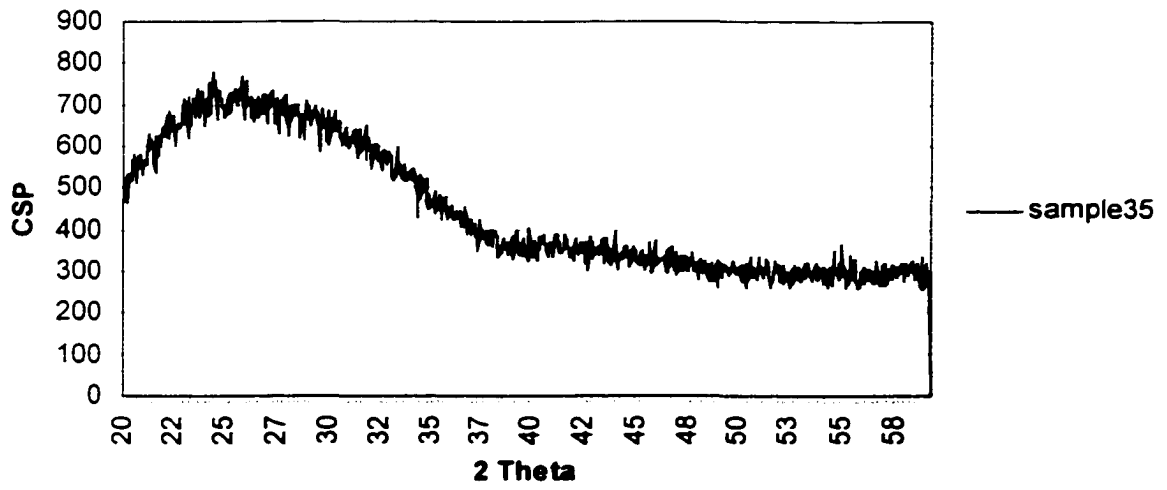


Figure 6.4.1 Counts vs 2θ for sample 35.

### XRD Results

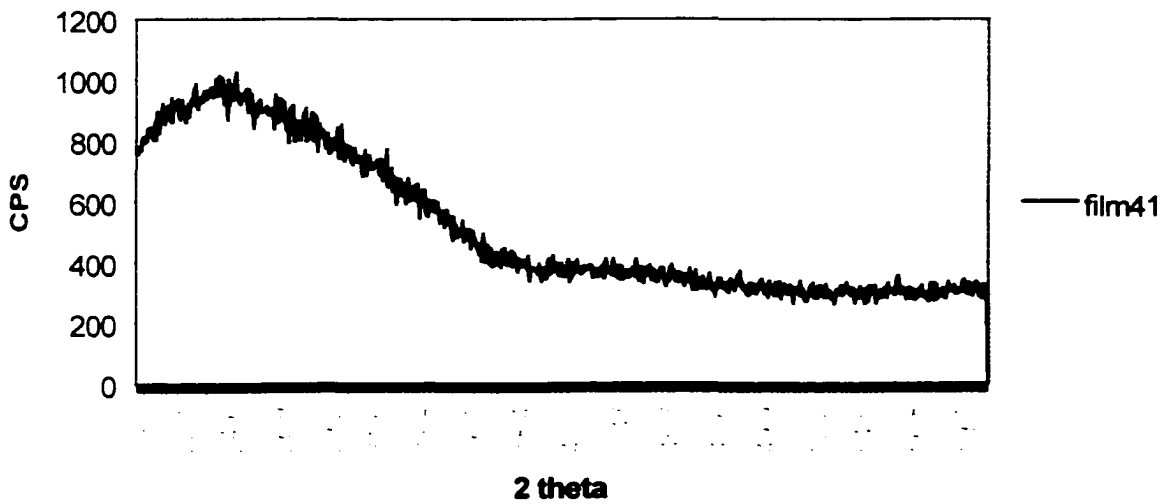


Figure 6.4.2 Counts vs 2θ for sample 41.

### XRD Results

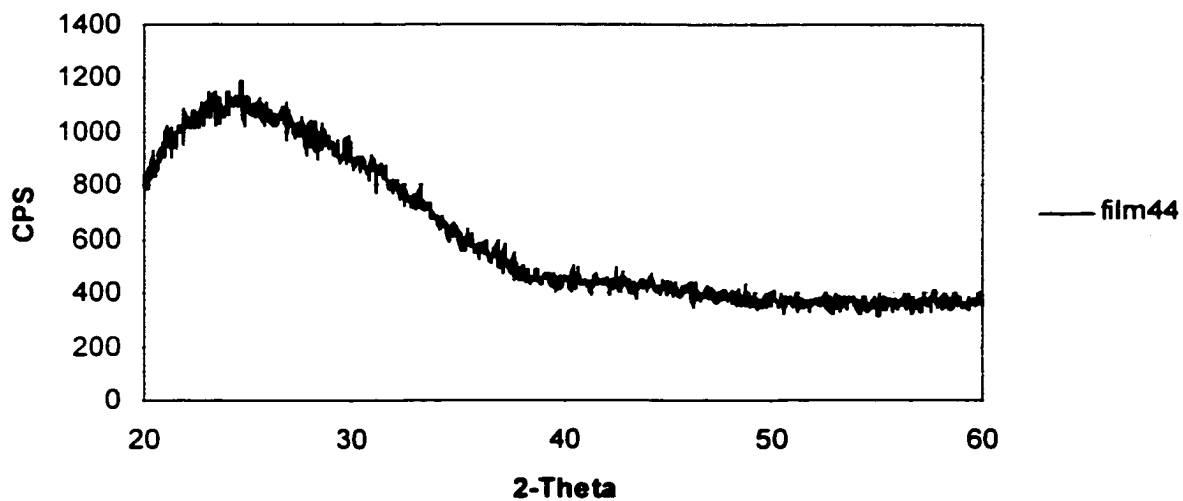


Figure 6.4.3 Counts vs  $2\theta$  for sample 44.

### XRD Results

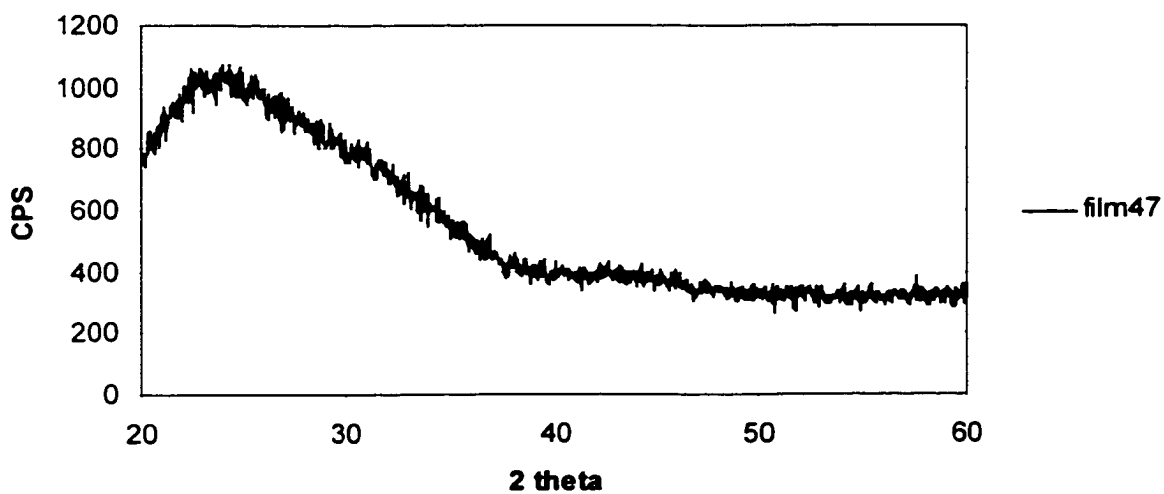


Figure 6.4.4 Counts vs  $2\theta$  for sample 47.

### XRD Results

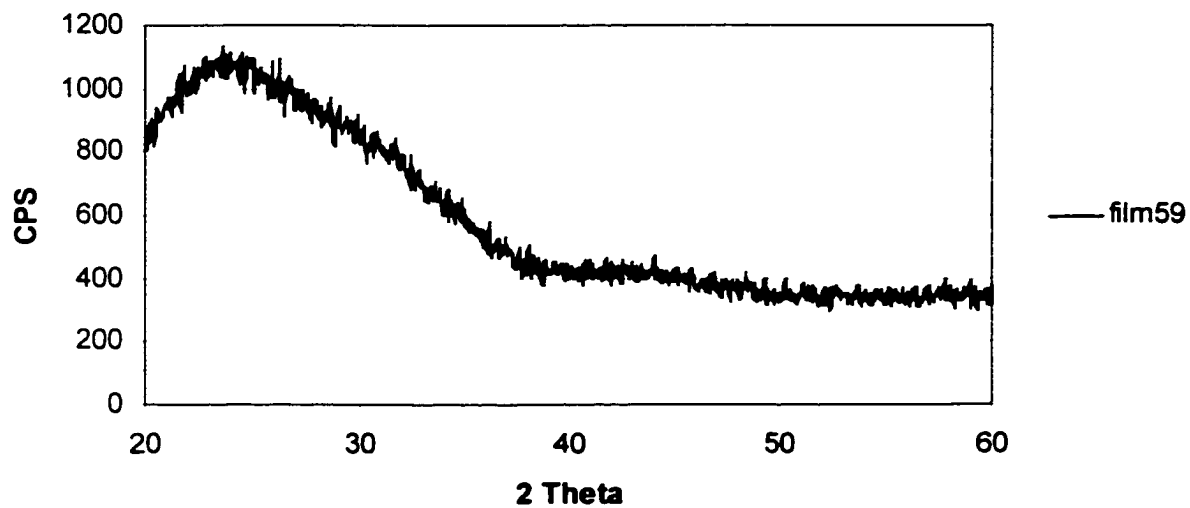


Figure 6.4.5 Counts vs  $2\theta$  for sample 59.

### XRD Results

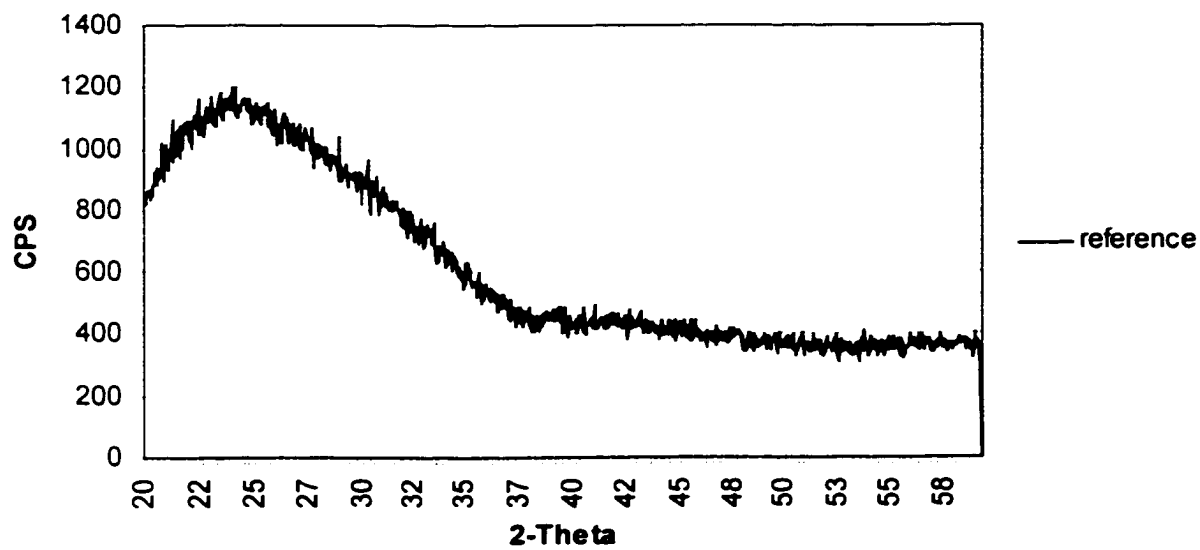


Figure 6.4.6 Counts vs  $2\theta$  for a plain quartz slide.

A substrate heater was not used. Rather, we chose to let the current to the sample determine the growth temperature. Although this factor was uncontrolled, the temperature never went above 80 C after 20 mins deposition. At 80 C, the temperature is nearly 300 C below the lowest temperature ever recorded for crystalline growth. It was hoped that the bombardment of charged species could have been enough to impart the necessary energy to show the potential for some crystal growth. This is clearly not the case. Nevertheless, we believe that with sufficient ion flux and proper heating to the substrate, it would be possible to repeat the results at the low temperatures reported by Schneider, *et.al*.

The mechanism attributed to crystal growth at this temperature is referred to as plasma activation. Due to the complicated experimental setup, which is similar to the one used herein, it was not possible to determine the exact mechanism responsible for crystal formation. Laser ablation has been used to activate an argon plasma in an attempt to quantify this effect. Hirschauer deposited crystalline  $\alpha$ -Al<sub>2</sub>O<sub>3</sub> and other materials difficult to deposit at substrate temperatures of 850 C by this technique.<sup>73</sup> Unfortunately, no systematic studies have been performed including some of the basic deposition parameters such as temperature and ion energy.

#### **6.4 Conclusion**

In this chapter, we have shown how to deposit alumina-like films with RF power using a solid target at rates that approach those of DC reactive magnetron. We have implemented changes that allow for longer processing times and increase repeatability and throughput. We show deposition rates approaching 200 A/min, which are

similar to those reported using a solid target. The compositions of the films grown were calculated to contain an Al/O<sub>2</sub> ratio close to ideal. The extra oxygen found in ESCA is believed to be chemically bound water molecules.

Comparing our results with the most recent reports we find rates as high as 76% of the solid metal or approximately 540 A/min (9 A/sec) rate using pulsed DC by Schneider *et.al*. Such result compares favorably to the data presented herein. We point out to the reader that such results obtained through reactive sputtering require complicated closed loop control of oxygen. Moreover, reactive DC sputtering of non-conductive oxides is an inherently unstable process that requires taking extraordinary precautions to prevent arcing. Our system is significantly easier to operate and is not limited to the above problems.

X-ray diffraction of as deposited films showed that they are all amorphous. This was not unexpected, since we did not use either a substrate heater or bias. We note that not all the films reported by Schneider are X-ray crystalline. In fact, most of them are not. This is an indication that achieving any measure of crystal order is very difficult.

Some hardness measurements were made on the thicker, clearer amorphous films and obtained hardness of the order of 5 GPa, which is significantly lower than the value of 20 GPa for the corundum standard. Hardness is defined as the average pressure under the indenter, calculated as a force divided by the projected area of contact between the indenter and the material. For the Vicker's diamond indenter, the projected area of contact is given by  $A = 26.46h_p^2$  where  $h_p$  is the indentation depth into the glass slides. The hardness is then calculated from the expression  $H = \frac{F}{A}$

where  $F$  is the applied force. A force of 15mN is selected to prevent the glass substrate contribution in plastic deformation, in accordance with the empirical rules which state that the indentation depth must not exceed one-seventh or one-tenth of the coating thickness.<sup>74</sup> Reports in literature for amorphous alumina prepared by ion bombardment is 10 GPa<sup>75</sup>, e-beam evaporation 8.4 GPa<sup>76</sup> and R.F. magnetron sputtering 9.5 GPa.<sup>77</sup> It is not obvious how to interpret the different hardness values. It may be explained by one or another of the following factors: microstructural changes, stress evolution, energetic neutral atom bombardment. In fact all these phenomena are closely linked, but their interdependence and respective roles in increase in hardness are difficult to identify. The increase in hardness of the coating with power has been reported for sputtered TiN.<sup>78</sup> It was explained by the increase in substrate bias and energetic atom bombardment as the power rises.

Film adhesion was generally good as measured qualitatively by the "sticky" tape method. The adhesion strength depends on both the bonding strength between the coating and the substrate, and the microstructure in the interface region.<sup>79</sup> The type of bonding may be covalent, Van Der Waals, electrostatic or a combination of these. It is likely that higher deposition energy of sputtered atoms as the plasma pressure decreases may induce more covalent interactions and improve adhesion. Bodino has shown that alumina coatings deposited on PET by rf magnetron sputtering lead to an interface with covalent interaction through Al-O-C bonds.<sup>80</sup> All this indicates that we have qualitatively good film adhesion that can be improved upon at lower pressures.

## Chapter 7 Suggestions for Further Study

The goal of this work was to build a novel source for RF sputtering from a solid target, and this goal was successfully achieved. The film rates were high, and the stoichiometry of the films was very nearly that of the ideal  $\text{Al}_2\text{O}_3$  ratio. Now it is necessary to learn to deposit  $\text{Al}_2\text{O}_3$  films with better hardness and crystallinity, which should be achieved with the use of bias and substrate heating.

There is sufficient circumstantial evidence that indicates that energetic particle bombardment helps drive crystalline growth at low temperature. Result of this so-called "plasma activation" has been shown by Schneider and by laser ablation by Hirschauer to obtain crystalline formation at low temperature. Of particular interest would be to explore the effects of the electron beam component on the crystalline growth dynamics. Given that ceramics have a large secondary electron emission coefficient, it should be possible to create an in-situ beam for this purpose. The author believes that this could be accomplished by studying the effects of He partial pressures on the gas mixture.

Because the field of electron beam is fairly mature, the above suggestion should be a straightforward implementation at low chamber pressures. Collins, et.al. has already shown the versatility of electron beams for annealing ion-implanted wafers without the redistribution of the original dopant profile.<sup>61</sup> Other potential applications shown by Collins et.al of these electron beams to semiconductor applications include thick resist exposure.<sup>62</sup> Using a similar setup as the one described herein for sputtering, Shaw and Collins have shown the ability to generate electron beams generated by ion-induced secondary electron emission.<sup>63</sup> The researchers found that the CCP set the ion impingement energy as well as the electron

beam acceleration. The ICP sets the current flux to the substrate much like Rossnagel had described earlier. A detailed study of the plasma interactions and effects of the electron beam intensity on the film properties would add much needed insight into the crystal growth mechanics.

The suggestion described on the previous paragraph would necessitate the addition of substrate bias to modulate the electron beam. The author would suggest the use of pulsed power to maintain the power dissipation to the substrate at a minimum while maintaining precise bias control. This would allow for exact heat control to the substrate through a heater, which may be needed to reduce the hydration of the alumina films.

## REFERENCES

- 
- <sup>1</sup> S.M. Rossangel and J. Hopwood, *Appl. Phys. Lett.*, 63 (24), 1993
- <sup>2</sup> S.M. Rossnagel and J. Hopwood, *J. Vac. Sci. Technol. B* 12 (1) Jan/Feb 1994
- <sup>3</sup> Hoffman, D.W., Thornton, J.A. *Thin Solid Films*, 40 (1977) 335
- <sup>4</sup> J.M. Schneider, W.D. Sproul, R.W.J. Chia, M.S. Wong, and A. Matthews, *Surf. Coat. Technol*, 96 (1997) 262-266.
- <sup>5</sup> M. Watanabe, D.M. Shaw, G.J. Collins, H. Sugai *Journal Appl. Physics*, Vol 85, N7 (1999)
- <sup>6</sup> M.A. Lieberman, A.J. Lichtenberg, "Principles of Plasma Discharges for Materials Processing," John Willey & Sons, New York, 1994
- <sup>7</sup> M. Tan, S Tan and Y Shen, *IEEE Trans. On Magnetics*, Vol 31, No 6, Nov, 1995
- <sup>8</sup> M. Tan, et. al. Nov. 1995
- <sup>9</sup> B. Chapman, *Glow Discharge Processes*, John Wiley & Sons, New York 1980
- <sup>10</sup> B. Chapman, 1980
- <sup>11</sup> B. Chapman, 1980
- <sup>12</sup> J.M. Schneider, et. al. (1997)
- <sup>13</sup> B. Bushan, B.K. Gupta, *Handbook of Tribology*, McGraw-Hill, New York, 1991
- <sup>14</sup> O. Knotek, F. Loeffler, W. Beele, *Surf. Coat. Technol.* 61 (1993) 6.
- <sup>15</sup> S. Zhu, F. Wang, H. Lou, W. Wu, *Surf. Coat. Technol.* 71 (1995) 9.
- <sup>16</sup> R. Cuffe, B. Baud, J.P. Besse, M. Jaquette, *Thin Solid Films* 266 (1995) 198.
- <sup>17</sup> Yamashita, M, 1989 *J. Vac. Sci. Technol. B* 7, 151
- <sup>18</sup> Rossnagel and Hopwood 1993
- <sup>19</sup> J.M. Schneider, et. al, (1997)

- 
- <sup>20</sup> Lieberman and Lichtenberg, 1994.
- <sup>21</sup> Holt, H.E., Haskill, R.E., Plasma Dynamics, McMillan, New York, 1965
- <sup>22</sup> Godyak, V.A. and Sternberg, N Phys. Rev., vol A42, 1990
- <sup>23</sup> Godyak, V.A., Soviet Radio Frequency Discharge Research. Falls Church, VA: Delphic, 1996
- <sup>24</sup> Godyak and Sternberg , 1990
- <sup>25</sup> Godyak, V.A, Piejak, R.B. Alexandrovich, B.M., IEEE Trans. Plasma Sci., Vol 19, 1990
- <sup>26</sup> Tykocinsky-Tykociner, Phil. Mag., 13, 1932
- <sup>27</sup> Piejak,R.B., Godyak, V.A. Alexandrovich, B. M. Plasma Sources Sci. Tech. , 1 1992
- <sup>28</sup> Piejak, Godyak and Alexandrovitch, 1992
- <sup>29</sup> Turner, M.M. Phys. Rev. Lett, Vol 71, N 12 p. 1844
- <sup>30</sup> Godyak, V.A., Piejak, R.B. , Alexandrovich, B.B. Plasma Sources Sci. Technol. 1, 36 (1992)
- <sup>31</sup> Druyvesteyn, M.J., Z. Phys. 64, 781 (1930)
- <sup>32</sup> E.M. Williams, Paper #AA-04, The 6<sup>th</sup> Joint MMM-Intermag. Albuquerque, NM, USA, June 1994, unpublished.
- <sup>33</sup> Sproul, W.D. Graham, M.E. Wong, M.S. Lopez, S. Li, D Scholl, R.A. J. Vac. Sci. Technol. A 13(3) May/Jun 1995
- <sup>34</sup> Sproul, W.D. Graham, M.E. Wong, M.S. Lopez, S. Li, D Scholl, R.A. J. Vac. Sci. Technol. A 13(3) May/Jun 1995
- <sup>35</sup> O. Knotek, F. Loeffler, W. Beele, Surf. Coat. Technol. 61 (1993) 6
- <sup>36</sup> S.K. Rutledge, B.A. Banks, J. Hunt, *Nasa Technical Memorandum 106966*, 1995
- <sup>37</sup> R. Cueff, B. Baud, J.P. Besse, M Jacquette, Thin Solid Films 266 (1995) 198
- <sup>38</sup> P. Liu and J. Skogosmo, Acta Cryst., B47 (1991) p.425.

- 
- <sup>39</sup> B.C. Lippens and JJ Steggerda, "Physical and Chemical Aspects on Absorbens and Catalysis," Academic Press., London, UK, 1970.
- <sup>40</sup> H.G. Prengel, W. Heinrich, G. Roder, and K.H. Wendt, Surf. Coat. Technol., 68/69, (1994) 217
- <sup>41</sup> O. Zywitzkina d G. Hoetssh, Surf. Coat. Technol., 86-87 (1996) 640.
- <sup>42</sup> AMS Handbook, Vol.1, "Properties and Selection: Iron Steels and High Performance Alloys," 134, 1990
- <sup>43</sup> E. Ryshkenwitch and D.W. Richerson, *Oxide Ceramics*, General Ceramics, Inc., Published by arrangement with Academic Press, Orlando, Fl. Haskell, NJ, 1985.
- <sup>44</sup> Vossen, J.L. J. Vac. Sci. Technol. 8 S-12 (1971)
- <sup>45</sup> Grantham, D.H. Paradis, E.L., Quinn, D.J. " A High Rate RF Sputtering System," 3<sup>rd</sup> Symposium of the Deposition of Thin Films by Sputtering, University of Rochester, 1969 (unpublished)
- <sup>46</sup> Cueff, R. Baud, G. Besse, J.P. Jacquest, M. Thin Solid Films 266 (1995)
- <sup>47</sup> Thornton, J.A., Ann Rev. Matter Sci. 7 (1977) 239
- <sup>48</sup> Schneider, J.M., Sproul, W.D. Voevodin, A.A. Mathews, A, J. Vac. Sci. Technol. A 15(3), May/Jun 1997
- <sup>49</sup> Voevodin A.A., Campano, M.A., Safriet, A.J. Donley, A.S. Zabinski, J.S., Appl. Phys. Lett., 69 (1996) 188.
- <sup>50</sup> G.K. Wehner and G.S. Anderson, in L.I. Maisel and R. Glang (eds.) "Handbook of Thin Film Technology," McGraw-Hill, New York, 1970
- <sup>51</sup> K. Tominaga, N Ueshiba, Y Shintani and O. Tada, Jpn. J. Appl. Phys., 20 (1981)
- <sup>52</sup> K. Tominaga, S. Iwamura, Y. Shintani, and O. Tada, Jpn. J. Appl. Phys., 21 (1982)
- <sup>53</sup> J. A. Thornton, J. Vac. Sci. Technol., 11 (1974) 666
- <sup>54</sup> R.S. Nowicki, J. Vac.Sci. Technol., Vol 14, No. 1 Jan/Feb. 1977

- 
- <sup>55</sup> R.S. Nowicki, Jan/Feb 1977 p. 128
- <sup>56</sup> R.S. Robinson, J. Vac. Sci. Technol., 16, 185 (1979)
- <sup>57</sup> M. Rossnagel and J. Hopwood, J. vac. Sci. Technol. B, Vol 12, No1, Jan/Feb 1994
- <sup>58</sup> Schneider, et. al. Surf. Coatings Technol, 96 (1997) 263
- <sup>59</sup> C.R. Brundle, C.A. Evans Jr, and S. Wilson, Encyclopedia of Materials Characterization, (Butterworth-Heinemann, Massachusetts, 1992), chapter 5.
- <sup>60</sup> C.J. Powell, et.al. Electron Spect. Rel. Phenom. 98-99 1-15 (1999)
- <sup>61</sup> Physical Electronics, Inc. 6509 Flying Cloud Drive, Eden Prairie, MN 55344
- <sup>62</sup> Caudron, E, Baud, G, Besse, J.P. Blondiaux, G, Jacquet, M. Solid State Ionics, 70/71 (1994) 629
- <sup>63</sup> Bhatia, C.S., Guthmiller, G. Spool, A.M., J. Vac. Sci. Technol., A7 (1989) 1928
- <sup>64</sup> Vuoristo, P., Mantyla, T., Kettunen, P. Thin Solid Films, 204 (1991), 297
- <sup>65</sup> Duchatelard, P. Baud, G. Besse, J.P. and Jacquet, M. Thin Solid Films 250 (1994) 142
- <sup>66</sup> Cueff, R. Baud, G. Besse, J.P. Jacquet, M. Thin Solid Films 266 (1995) 201
- <sup>67</sup> M. Watanabe, private communication, CSU Electrical Engineering Dpt, 1999
- <sup>68</sup> J Schneider,, W. Sproul, A Voevodin, and A. Matthews, J. Vac. Sci Technol. A 15 (3), May/Jun 1997.
- <sup>69</sup> Frieser, R.G., J. Electrochem. Soc. 113 (1966) 357.
- <sup>70</sup> Thornton, J.A, Chin, J. Ceramic Bull. 56 (1977) 504
- <sup>71</sup> Jaemting, A., Ring, M. Ruppi, S, Swain, M.V., J. Hard Matter, 6, 67 (1995)

- 
- <sup>72</sup> D. Grier, G. McCarthy, North Dakota State Univeristy, Fargo, ND, ICDD Grant-in-Aid (1991)
- <sup>73</sup> Hirschauer, B. Soderholm, S. Chiaia, G. Karlsson, U.O., Thin Solid Films, 305 (1997) 243-247.
- <sup>74</sup> Jehn, H. Galvanotechnik, 80 (1989) 1193
- <sup>75</sup> Oliver, W.C., McHArgue, C.J., Thin Solid Films, 161 (1988) 117
- <sup>76</sup> Steinwell, J.E., Johnson, H. Mater. Res. Soc. Symp. Proc., 120 (1988) 193
- <sup>77</sup> Chou, T.C., Adamson, D., Mardingly, J, Nieh, T.G., Thin Solid Films, 205 (1991) 131
- <sup>78</sup> Sproul, W.D., Rudnik, P.J., Thin Solid Films, 171 (1989) 171
- <sup>79</sup> Bunshah, R.F., Deposition Technologies for Thin Films and Coatings, Noyes, New Jersey, 1982
- <sup>80</sup> Bodino, F., Baud, G. Benmslek, M., Besse, J.P., Dunlop, H.M., Jacquet, M., Thin Solid Films, 241 (1994) 21
- <sup>81</sup> Moore, C.A. Rocca, J.J. Johnson, T and Collins, G.J. Appl. Phys.Lett, vol 43, (3) (1983) 290-292
- <sup>82</sup> Krishnaswamy, J, Li, L, Collins, G.J, Hiraoka, H. Caolo, M.A. J. Vac. Sci. Technol. B Vol. 8 (1) (1990) 39-46
- <sup>83</sup> Shaw, D. Watanabe, M. Collins, J.G. Sugai, H. Jap. J. Appl. Phys. Part 1 Vol 38 (7B) (1999) 4590-4594

---

**APPENDIX**

On chapter 6 we described changes to the chamber and ran a set of deposition experiments based on the regression results obtained from the first configuration. The raw data for chapter 6 is presented below on table A1.

Table A1 Details of the runs for the second set of experiments

Run	pressure (mT)	ccp (W)	icp (W)	Ar	O2	Notes
33	10	400	0	100%	0%	OK
34	10	500	0	100%	0%	OK
35	10	600	0	100%	0%	OK
36	10	0	100	100%	0%	OK
37	10	0	200	100%	0%	OK
38	10	0	300	100%	0%	OK
39	10	400	100	100%	0%	OK
40	10	500	100	100%	0%	OK
41	10	600	100	100%	0%	OK
42	10	400	200	100%	0%	residual N2
43	10	500	200	100%	0%	residual N2
44	10	600	200	100%	0%	OK
45	10	400	300	100%	0%	OK
46	10	500	300	100%	0%	OK
47	10	600	300	100%	0%	OK
48	10	400	0	98%	2%	over by 30 sec.
49	10	500	0	98%	2%	5% reflected power. Fixed match on ICP
50	10	600	0	98%	2%	OK
51	10	400	100	98%	2%	OK
52	10	500	100	98%	2%	OK
53	10	600	100	98%	2%	OK
54	10	400	200	98%	2%	OK
55	10	500	200	98%	2%	OK
56	10	600	200	98%	2%	OK
57	10	400	300	98%	2%	OK
58	10	500	300	98%	2%	OK
59	10	600	300	98%	2%	OK
60	10	400	0	96%	4%	OK
61	10	500	0	96%	4%	OK
62	10	600	0	96%	4%	OK
63	10	400	100	96%	4%	OK
64	10	500	100	96%	4%	OK
65	10	600	100	96%	4%	OK
66	10	400	200	96%	4%	OK
67	10	500	200	96%	4%	OK
68	10	600	200	96%	4%	OK
69	10	400	300	96%	4%	OK
70	10	500	300	96%	4%	OK
71	10	600	300	96%	4%	OK

We also explained the theory for Langmuir probes in section 3.2 and briefly went over the details for making one of these probes. We used a planar probe with automated data acquisition with Labview to obtain a better understanding of the plasma characteristics before running any experiments. The data obtained from those observations is indicated below on table A2

Table A2. Langmuir probe measurement obtained on 100% Ar plasma.

0	1 ICP	2 CCP	3 PRESS	4 ARGON	5 VP	6 VF	7 DENSITY	8 TE
1		300	15	10	38.15	19.06	3.87e+10	3.67
2	400	500	15	20	37.54	19.42	4.92e+10	3.48
3	200	100	18	15	37.71	20.16	1.61e+10	3.38
4	200	500	20	10	45.16	23.12	2.58e+10	4.24
5	300	500	18	20	38.45	20.66	4.01e+10	3.42
6	200	500	20	20	42.50	23.18	2.87e+10	3.72
7	400	500	20	10	39.40	20.40	4.01e+10	3.64
8	200	100	15	10	39.60	22.10	1.45e+10	3.40
9	400	100	18	20	33.88	16.81	4.77e+10	3.28
10	300	100	15	20	34.10	16.40	2.97e+10	3.40
11	400	100	15	15	30.80	15.10	3.87e+10	3.10
12	200	500	15	10	42.41	22.43	2.58e+10	3.84
13	200	300	20	10	39.45	21.34	2.17e+10	3.48
14	400	100	20	10	34.90	17.53	3.84e+10	3.35
15	300	100	20	15	35.61	17.89	2.98e+10	3.41
16	400	500	20	15	41.92	21.01	5e+10	4.02
17	300	300	18	10	38.30	20.93	2.84e+10	3.34
18	400	300	20	20	35.26	17.50	5.44e+10	3.41
19	200	300	15	20	39.65	22.23	2.16e+10	3.35
20	200	100	20	20	35.66	17.78	2.11e+10	3.44